



Displaced track finding efficiency and detecting new long-lived particles at Belle II

Daniel Marcantonio

Under the supervision of A/Prof. Phillip Urquijo

A thesis submitted in partial fulfillment
of the requirements for the degree of
Master of Science (Physics)
THE UNIVERSITY OF MELBOURNE

November 2020

Abstract

There are numerous extensions to the Standard Model that introduce new particles that have long lifetimes, corresponding to a flight length of centimetres or more in a particle collider. No such particle has yet been found, with searches often being limited statistically. The high luminosity that the SuperKEKB collider provides the Belle II experiment allows grants greater statistical power in these searches than ever before, making Belle II the most sensitive experiment to date in detecting new long-lived particles in the mass range of a few Gev/c^2 .

In this thesis, we use Monte Carlo simulations to lay the foundations for a search for long-lived particles. To construct an accurate search, precise understanding of how well the Belle II detector tracks charged particles that originate far from the interaction point is essential. We perform a measurement of displaced track finding efficiency for the first time in the Belle II experiment, using a method involving the partial reconstruction of D^{*+} decays. From the result of the tracking study, combined with the outcome of the long-lived particle search we construct, we provide the most accurate estimate of Belle II's sensitivity to new long-lived particles to date.

Statement of Contribution

Chapter 1 contains an original literature review, introducing the theoretical framework of the Standard Model as well as some extensions to it, and a review of relevant previous searches for new particles. Chapter 2 gives an overview of the Belle II detector hardware, and introduces a few key software features used including particle identification variables and vertex fitting.

The rest of this thesis contains original work. Chapters 3 and 4 explore what decay topologies with long-lived particles would look like in the Belle II detector, and describe some key selection criteria that can be used to discriminate these events from background events. Chapter 5 details a novel method of estimating the track finding efficiency at Belle II, and uses data taken in 2019. Chapter 6 combines results from the previous three chapters in order to provide an updated estimate to Belle II's sensitivity to long-lived particles.

Acknowledgements

I would like to thank A/Prof. Phillip Urquijo for the support he has provided me over the last two years. His depth of knowledge and ability to pass on wisdom to others are a continuing source of inspiration. Many thanks to Cate for giving up lots of time this year to teach me how to do research, and to Daniel for always going to extra mile to make sure I understood what he was explaining to me. My excellent proofreaders Daniel, Marcel, Elodie, Kat and Ayo; thank you for your scrutiny and (sometimes) harsh words, they were exactly what proofreaders should provide. I assure you that any mistakes you might find in this work were introduced after your keen eyes read it.

To my friends in the barn, you were the both the most unexpected and the best thing I gained from this course. I am thankful for your constant support and affection, and will cherish the fun we had over the last two years.

To mum, dad, Oscar, Anastasia and Buckley, thank you for your unwavering faith in me, I shudder to think how this thesis would have turned out had it not been for your support. To everyone that helped me along the way; this work is as much your accomplishment as it is mine.



SCHOOL OF PHYSICS

COVID-19 Impact Statement

In response to COVID-19, The University of Melbourne transitioned to a working at home model, closing all buildings on 30th March. If the restrictions imposed by the COVID-19 pandemic have affected your research and therefore your ability to complete your research/thesis as planned, then please provide details below of these impacts so that your examiner(s) may factor these into their assessment. Please complete this form in conjunction with your supervisor and submit this along with your thesis.

Student name: Daniel Marcantonio

Date: 12th of November 2020

Supervisor(s) name: A/Prof. Phillip Urquijo

When completing each section below please state i) the impact and ii) the consequences to your research report/thesis. For guidance of the type of expected response, please refer to the Impact Thesis Statement Exemplar.

Preamble/Synopsis

My research project focused on measuring tracking and reconstruction efficiencies for the Belle II experiment. The physical shutdown of the University of Melbourne occurred in my third semester of research project, affected 75 points of enrolment in total. Accessing advice on how to use the Belle II Software Framework, ROOT, and on how to do research in general was more difficult as all communication was done online.

Field work

N/A

Laboratory experiments

N/A

Data analysis

Impact:

All of the data that I used in my project is stored on external computing systems that I had to access remotely. Even with the best possible internet plan available at my address, my connection suffered from frequent (once every day or two) drop outs

which could result in lost work or generally slow down the pace at which I could work, as I would need to load in datasets again when the connection came back online.

Consequences to research report:

Whilst it is hard to quantify time lost, I was certainly left with much less time to properly develop the final chapter and conclusion of my thesis.

Thesis writing

Impact:

1. Less contact with supervisors and peers
2. Less than ideal working from home environment

Consequences on report:

1. In a normal situation, I would be able to drop into my supervisor's office at any time and discuss my project. Although we did have scheduled meetings on Zoom multiple times a week, the online-only supervision resulted in less interaction overall. Being in an office surrounded by peers is a fantastic environment for learning, but the lockdown made that kind of environment impossible to access. This increased the amount of time I had to spend on several tasks, including learning new pieces of code and learning a new concept in physics that the project required. This added to the overall time I had to spend on my research, cutting into the time I had to write my report.
2. As I was working from home, I did not always have a quiet environment to work in, and it was generally harder to stay on task because the home/work separation was gone.

Comments from supervisor(s)

Daniel's MSc project has been affected by the working from home model. His MSc is based on analysis of large datasets from the Belle II experiment in Japan, demanding high bandwidth for many aspects of his project. This has been adversely affected by the nature of working from home rather than on the University network. Ultimately this slowed down progress. He has also suffered indirect effects of working on a highly complex experiment without as much day to day feedback from peers and research staff as one would ordinarily receive.

Contents

1	Introduction	1
1.1	New long-lived particles	1
1.1.1	Higgs-like production of dark scalars	2
1.1.2	Long-lived particles from axion-like particle production	2
1.1.3	Decays of dark scalars	3
1.2	Searches for long-lived particles	3
1.2.1	Electron-positron collider searches	4
1.2.2	Hadron collider searches	5
1.2.3	Searches at fixed target experiments	6
1.2.4	Future searches	6
1.2.5	Summary of previous searches	7
1.3	The role and scope of this analysis	8
2	The Belle II Experiment	9
2.1	The SuperKEKB Collider	9
2.2	Belle II Detector Components	9
2.2.1	Vertex Detector (VXD)	10
2.2.2	Central Drift Chamber (CDC)	10
2.2.3	Particle identification system (TOP and ARICH)	11
2.2.4	Electromagnetic Calorimeter (ECL)	11
2.2.5	K_L^0 - Muon Detector (KLM)	11
2.2.6	Trigger system	11
2.2.7	Charged particle identification variables	12
2.3	Vertex Fitting	12
2.3.1	Global decay chain vertex fitting	12
2.3.2	Tree Fitter	13
2.3.3	Constraining a decay chain	13
3	Monte Carlo simulation of long lived particles	14
3.1	MC Generation	14
3.2	Dimuon kinematic distributions	14
3.3	Sensitivity to displaced decay products	15
4	Preparing a search for new long-lived particles	17
4.1	Background processes	17
4.2	Higgs-like channel	18
4.2.1	Reconstruction	18

4.2.2	Higgs-like channel efficiency	20
4.3	ALP channel	22
4.3.1	Selection criteria	22
4.3.2	ALP channel efficiency	22
4.4	Vertex fitting resolution on long-lived particles	23
5	Displaced track finding efficiency	25
5.1	Tracking at Belle II	25
5.1.1	Charged particle reconstruction	25
5.1.2	V^0 -like particle reconstruction	27
5.2	Measuring track finding efficiency using partially reconstructed D^* decays	27
5.2.1	Reconstruction	28
5.2.2	Partial reconstruction method	30
5.2.3	Constructing a scan	32
5.2.4	Fitting the D^{*+} mass distribution	33
5.2.5	Results	35
6	Sensitivity to long-lived particles at Belle II	39
6.1	Limiting factors	39
6.2	Dark scalar sensitivity limits	39
7	Conclusion	43
	Bibliography	44

Chapter 1

Introduction

The Standard Model of particle physics (SM) details the fundamental constituents of matter and their interactions, and is one of the most rigorously tested theories in science. It explains the strong, weak, and electromagnetic forces through mediator particles or gauge bosons; the gluon (g), photon (γ) and W^\pm and Z^0 bosons. The SM fermions come in two types; quarks and leptons. There are six quarks, up (u), down (d), charm (c), strange (s), top (t), and bottom (b), and six leptons, the electron and electron neutrino (e and ν_e), muon and muon neutrino (μ and ν_μ) and the tau and tau neutrino (τ , and ν_τ). Each of these fermions has a corresponding antiparticle with quantum numbers of equal magnitude and opposite sign. Interaction between fermions are mediated by the gauge bosons, which have conserved charges associated with different gauge groups. The Z^0 , W^\pm , and γ mediate the electroweak force and are charged under $U(1)_Y$ and $SU(2)_L$ gauge groups. The gluon is charged via an $SU(3)_C$ gauge group. Combined, these form the $U(1)_Y \otimes SU(2)_L \otimes SU(3)_C$ gauge group of the SM.

We do not find free quarks in nature; they are always in bound states consisting of two or three quarks. Two-quark bound states are called mesons, while three-quark bound states are called baryons. In this work, we are motivated by a number of theoretical extensions to the Standard Model that can be explored in the decays of mesons containing heavy quarks such as the charm and bottom quarks. The particles introduced in these extensions could be dark matter candidates, or mediate interactions between Standard Model and dark matter particles. Dark matter accounts for about 85% of the matter in the universe, yet we have never directly observed it, its existence has only been inferred through measurements of its gravitational effects [1–4]. We do not know what it consists of, or how it interacts with itself or visible matter. It does not interact with electromagnetism, and so we are left to probe it with the three remaining fundamental forces. There exist a multitude of theories that explain dark matter and its interactions, however none of these have yet been proven by experiment.

1.1 New long-lived particles

In 2012, the ATLAS and CMS experiments confirmed the existence of the Higgs boson [5]. To date, this is the only fundamental scalar boson we have found in nature. However, other scalars could exist. Here, we briefly introduce models that propose new long-lived particles as motivation for the search that will be presented in the latter part of this work.

Extensions to the Standard Model introduce a scalar that mixes with the Higgs boson, offering solutions to unsolved problems in both particle physics and cosmology. For example, light scalar particles are thermal dark matter candidates or mediate interaction in the dark sector or between SM and dark section particles. Furthermore, they could facilitate baryogenesis or generate the electroweak hierarchy through cosmological relaxation. The SM can be extended by a real scalar field ϕ and a Dirac fermion χ , where both are strong and electroweak singlets [6]. The fermion is a stable dark matter candidate that does not mix with neutrinos as is it charged under \mathbb{Z}_2 symmetry. The introduction of these fields gives a Lagrangian with the following mass and interaction terms (ignoring a possible quartic interaction as we can only probe interactions that include fermion pairs):

$$\mathcal{L} = -\frac{1}{2}m_\phi^2\phi^2 - \lambda_3 |H|^2 \phi - y_\chi \bar{\chi}\chi - \frac{1}{2}m_\chi \bar{\chi}\chi, \quad (1.1)$$

where y_χ is the dark fermion coupling and λ_3 is a coupling constant.

A new force between the Higgs field H and the dark fermion χ is mediated by the scalar field. After electroweak symmetry breaking, the scalar ϕ and the neutral component of the Higgs field mix into two physical scalars; the 125 GeV Higgs boson h , and a new dark scalar S . The couplings of these physical scalars to fermions is given by

$$\mathcal{L}_y = y_\chi (s_\theta \bar{\chi}\chi h - c_\theta \bar{\chi}\chi S) - \sum_f \frac{m_f}{v} (c_\theta \bar{f}f h - s_\theta \bar{f}f S), \quad (1.2)$$

where s_θ and c_θ are the sine and cosine of the mixing angle θ . Through this, the dark scalar S inherits the couplings of the Higgs boson h to the SM fermions f , and will therefore couple more strongly to heavier fundamental fermions.

1.1.1 Higgs-like production of dark scalars

Dark scalars couple more strongly to more massive fundamental particles, and so they are more easily produced in interactions involving the third-generation quarks, and so can be produced abundantly through B meson pairs at the $\Upsilon(4S)$ resonance at SuperKEKB. The small coupling to the electron (due to its small mass) heavily suppresses the direct production of S through e^+e^- collisions. The production of dark scalars in B decays proceeds through a flavour-changing current with a top-quark loop (Figure 1.1a), inducing a two body decay $B \rightarrow MS$ where M is any scalar, pseudoscalar or vector meson such as π, K, D or ρ .

1.1.2 Long-lived particles from axion-like particle production

Axion-like particles (ALPs) are another particle predicted by Standard Model extensions that could be long-lived. In general, ALPs can couple to electroweak gauge bosons [7], Standard Model fermions [8], gluons [9] and even the Higgs boson [10]. Furthermore, there are ALP models that can produce long-lived particles [11]. Decay topologies containing heavy quark decays into long-lived particles are therefore of interest when studying ALPs. In this thesis, we work under the assumption that ALPs couple to only $u\bar{u}$ and $d\bar{d}$, allowing ALPs to be produced in tree level processes in B^0 to \bar{D}^0 transitions [12], however the decay topology explored is relevant to a number of models.

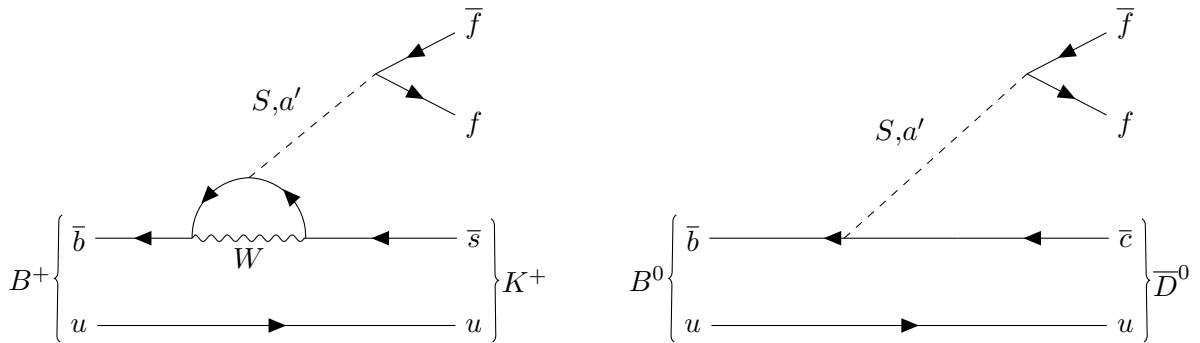


FIGURE 1.1: Feynman diagrams for the production of a dark scalar S or axion-like particle a' in a penguin-level process (a) and tree-level process (b).

1.1.3 Decays of dark scalars

The decay width of the dark scalar Γ_S can be split into partial widths of decays into SM particles and dark fermions once the dependence on the mixing angle θ is factored out:

$$\Gamma_S = s_\theta^2 \Gamma_{\text{SM}} + c_\theta^2 \Gamma_{\chi\chi}. \quad (1.3)$$

Decays into SM fermions dominate below the kinematic threshold $m_S = 2m_\chi$, as particles cannot decay into particles with combined masses greater than their own. For $m_S > 2m_\chi$, decay into dark fermions are possible, and so there are more decays which we cannot detect directly. The scalar can decay into final states with SM leptons or light mesons when its mass is in the GeV range. We don't know the m_S , however for a study at the Belle II experiment, the upper limit on m_S is a few GeV (this will be discussed in more detail in Chapter 6).

The decay width of S into SM particles increases with θ , and so we expect less S to be produced when θ is small. However, the fact that Belle II will produce more B meson pairs than any previous experiment means that it will be able to probe smaller couplings than previous experiments, as a larger dataset means a higher chance of observing rare decays.

For a mixing angle of $\theta = \frac{\pi}{2}$, the partial decay width to dark fermions goes to zero and the scalar will always decay into visible final states consisting of SM particles. The scalar's nominal lifetime is approximately $c\tau_S = c/\Gamma_S \approx s_\theta^{-2}$ nm. For a small mixing angle, the $s_\theta^2 \Gamma_{\text{SM}}$ term will be small and therefore the scalar will have a long lifetime compared to the scale of a detector. For example, $\theta = 10^{-4}$ corresponds to a lifetime $c\tau_S = 10$ cm, which is a length comparable to the radius of the silicon vertex detector (SVD) at Belle II. Long-lived scalars decaying into visible SM particles can leave obvious signatures in a detector as their daughter particles have displaced production vertices. Important scalar decays for searches are $S \rightarrow \mu^+\mu^-, e^+e^-, \pi^+\pi^-, K^+K^-, 4\pi$ or $4K$. Currently there are no processes in nature which can produce pairs of leptons of different types. As S is not a SM particle, it need not obey lepton universality, so $\mathcal{B}(S \rightarrow \mu^\pm e^\mp)$ may be non-zero.

1.2 Searches for long-lived particles

A number of searches for long-lived particles beyond the SM have been performed, but as of yet nothing has been found. However, constraints have been placed on the dark scalar mass and the

mixing angle between the dark scalar by BaBar and LHCb (see Figure 1.3). A number of both collider and fixed target experiments with different approaches and sensitivities have conducted searches.

In broad terms, they can be put into two categories: searches for invisible scalar decays and searches for visible scalar decays. The former assumes the scalar decays predominantly into dark sector particles $B \rightarrow KS(\rightarrow \chi\bar{\chi})$. These analyses proceed in a similar manner to searches for neutrinos, using missing energies to infer the presence of an undetected particle. Visible decay contributions come from the scalar decaying into SM particles such as muon, electron, or meson pairs.

1.2.1 Electron-positron collider searches

The production rate of scalars from e^+e^- annihilation is low, however B factories (collider experiments designed to produce B meson pairs) such as BaBar and Belle produced 550 million [13] and 770 million [14] B meson pairs respectively, which could readily produce long-lived particles through their decays. The large datasets of these experiments is one of the main factors that allowed them to probe smaller couplings to new particles. A drawback of these experiments is their efficiency in reconstructing high quality displaced vertices. Event reconstruction with vertex displacement that is macroscopic with respect to the detector often fails due to poor vertex quality. These events are rejected as misidentified events in many cases.

A study of dimuon decays at the Belle experiment presented in 2010 searched for a low mass pseudoscalar particle X in the 100 MeV/ c^2 mass range [15]. No significant signals were observed in the decay modes $B^0 \rightarrow K^{*0}X$, $K^{*0} \rightarrow K^+\pi^-$, $X \rightarrow \mu^+\mu^-$ and $B^0 \rightarrow \rho^0X$, $\rho^0 \rightarrow \pi^+\pi^-$, $X \rightarrow \mu^+\mu^-$. The models motivating the analysis predicted X to have a lifetime of 10^{-14} s. This analysis was found to have the same efficiencies for all lifetimes below 10^{-12} s as the primary vertex (that of the B^0) and secondary vertex were indistinguishable at lifetimes this small. The analysis saw a difference in efficiency of about 1% when the assumption was made that the muon tracks originate from the B^0 vertex compared to the secondary vertex. At lifetimes this short, the muon pairs are still produced close to the IP, and so they will cross most (if not all) of the detector material.

The only dedicated study of long-lived scalars at B -factory experiments to date was carried out at BaBar in 2015 [16]. Previously, long-lived scalars in the few GeV/ c^2 region had hardly been explored, especially in the context of a heavy-flavour environment. An inclusive search for displaced production vertices of charged leptons, pions, and kaons was carried out. The sensitivity of this search is significantly limited by hadronic backgrounds including pion and kaon decays. Background suppression was mainly achieved through two-body decay kinematics, as well as the requirement of a displaced vertex. The study placed 90% confidence level (CL) upper limits on $\sigma(e^+e^- \rightarrow SX)\mathcal{B}(S \rightarrow f)$ and $\mathcal{B}(B \rightarrow SX_S)\mathcal{B}(S \rightarrow f)$ where $f = e^+e^-, \mu^+\mu^-, e^\pm\mu^\mp, \pi^+\pi^-, K^+K^-,$ or $K^\pm\pi^\mp$. Note the electron-muon final state in the search. This decay channel would see minimal background as there are no standard model processes that produce such a final state. This study set a 90% CL upper limit on $\sigma(e^+e^- \rightarrow SX)\mathcal{B}(S \rightarrow \mu^+\mu^-)\epsilon(\mu^+\mu^-) \simeq 10^{-3}$ for a 2 GeV/ c^2 scalar using $\Upsilon(4S)$ and off-resonance data, where $\epsilon(f)$ is the efficiency for the final state f . Generally, inclusive searches, which search in a number of channels, cannot reject as much background as exclusive searches, which only search in a specific channel.

The study presented their results in two sections, a “model-independent” part, where there were no assumptions made about the production mechanism of the scalar, and a “model-dependent” section providing limits on the branching fraction for $B \rightarrow X_S S$ where X_S is any strange meson. For both cases, 90% CL upper limits for product of the production cross section and branching fraction were presented for $c\tau_S = 1, 2, 3, 20,$ and 100 cm over a range of masses (see Figure 1.2).

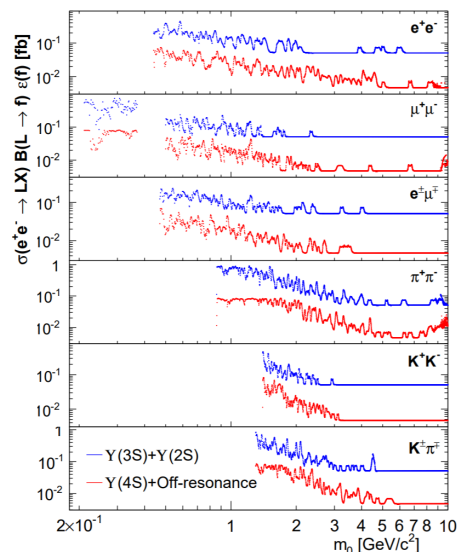


FIGURE 1.2: The 2015 BaBar study’s 90% CL upper limits on $\sigma(e^+e^- \rightarrow SX)\mathcal{B}(S \rightarrow f)\epsilon(f)$ as a function of S mass for two data samples, $\Upsilon(4S) + \text{off-resonance}$ (red) and $\Upsilon(3S) + \Upsilon(2S)$ (blue). The limits include the systematic uncertainties from the signal yield. The large fluctuations in cross section indicate that there was poorly controlled background, something that an exclusive analysis would be able to mitigate more than an inclusive analysis like this one. Note that in the figure (and the rest of the BaBar paper), the scalar is referred to as L , not S .

In 2013, Belle presented a search for another long-lived particle, a heavy neutrino [17]. Despite the final state particles being different to the dark scalar searches, i.e. one lepton ($\nu_\ell \rightarrow \ell\pi$), the displaced vertex and similar background makes the search similar enough to a dark scalar search that it is of interest. The common backgrounds include K_S^0 and Λ decays, as well as photon conversions into electrons displaced from the IP. Rejection of background involved requiring a different number of silicon vertex detector hits based on the displacement of the neutrino’s decay vertex, as well as using likelihood estimates to identify or veto tracks as particles. By considering the event kinematics and cutting around the invariant mass window of the search, background was reduced from $\sim 10^6$ events to a ‘handful’.

1.2.2 Hadron collider searches

The LHCb collaboration has conducted multiple searches for displaced vertices in $b \rightarrow s$ transitions using pp collision data. In 2015 a search for a new boson in $B^0 \rightarrow K_0^* \mu^+ \mu^-$ decays was presented [18], motivated by the good sensitivity provided by a top quark loop mediating $b \rightarrow s$ transitions. In 2017, another search was presented, this time for long-lived scalars [19]. The search claims to be sensitive to bosons with lifetimes up to 1000 ps ($c\tau = 30$ cm), however this seems to be quite a high estimation of the sensitivity of LHCb, as the high centre-of-mass energy means B mesons are boosted, and they and their decay products are far more displaced than at a B -factory.

In the 2015 search, a dimuon mass distribution was scanned for a resonance indicative of a new particle. The muon production was allowed to be displaced, but it was not a requirement of the search. The 2017 search for long-lived scalars at LHCb studied the decay $B^+ \rightarrow K^+ S$ with $S \rightarrow \mu^+ \mu^-$ using an integrated luminosity of 3 fb^{-1} at centre-of-mass energies $\sqrt{s} = 7$ and 8 TeV. A mass range of $250 < m_S < 4700 \text{ MeV}/c^2$ was searched, along with a lifetime range $0.1 < \tau_S < 1000$ ps, which corresponds to $0.003 < c\tau_S < 30$ cm. In this study, the scalar S was required to ‘decay within

a distance of about 60 cm' from the pp IP. This search excluded scalar mixing down to $\theta \simeq 10^{-4}$ using $B^+ \rightarrow K^+ S(\rightarrow \mu^+ \mu^-)$ decays, but with veto regions around the K_S^0 , $\psi(2S)$, and $\psi(3770)$ resonances. The 2015 LHCb study also vetoed the same regions.

Many of the strategies used in these searches are applicable to a search for long-lived particles at the Belle II experiment, including rejecting background using vertex displacement and two-body kinematics, and creating veto regions around the masses of known particles that can produce displaced vertices such as the K_S^0 .

1.2.3 Searches at fixed target experiments

In addition to collider searches, there have been searches for new scalar particles at fixed target experiments. The CHARM Collaboration used a 400 GeV proton beam on a thick copper target to search for new scalar particles in 1985 [20]. Candidates were chosen when the axion decayed into $\gamma\gamma$, e^+e^- , or $\mu^+\mu^-$. For all decay modes, no candidates were found.

1.2.4 Future searches

There are a number of proposed experiments dedicated to long-lived particle searches such as the SHiP (Search for Hidden Particles), CODEX-b (Compact Detector for Exotics at LHCb), FASER 2 (ForwArd SEArch expeRiment at the LHC 2) and MATHUSLA (MAssive Timing Hodoscope for UltraStable neutraL pArticles) experiments [21]. The latter three would be located at LHC IPs (i.e they would be collider experiments), while SHiP would be a fixed target experiemnt at the beam dump facility. A study late in 2019 compared the sensitivities to dark scalars of these experiments to that of LHCb, BaBar and Belle II [6].

Belle II can probe smaller mixing angles than either BaBar or LHCb, and in a displaced τ pair search, can access higher masses than any of the dedicated experiments. Furthermore, the range of masses and mixing angles Belle II can probe is far greater than the area that BaBar excluded in its search. However, it cannot probe mixing angles smaller than $\theta \approx 10^{-5}$, whereas MATHUSLA has a predicted sensitivity to angles below 10^{-6} due to its massive detector volume and displacement of at least 100m from the ATLAS or CMS interaction points, allowing it to observe much longer-lived particles. Studies also show Belle II covers a wide range of parameter space in searches for long-lived ALPs [22]. It should be noted, however, that these are estimates that fail to take into account the reconstruction efficiency at Belle II. In figure 1.3, the green shaded area shows the region of parameter space with at least $N_{\mu\bar{\mu}} = 3$ with 100% reconstruction efficiency and zero background events. However, they note that even with the presence of background events, the θ sensitivity only decreases by a factor of 2.

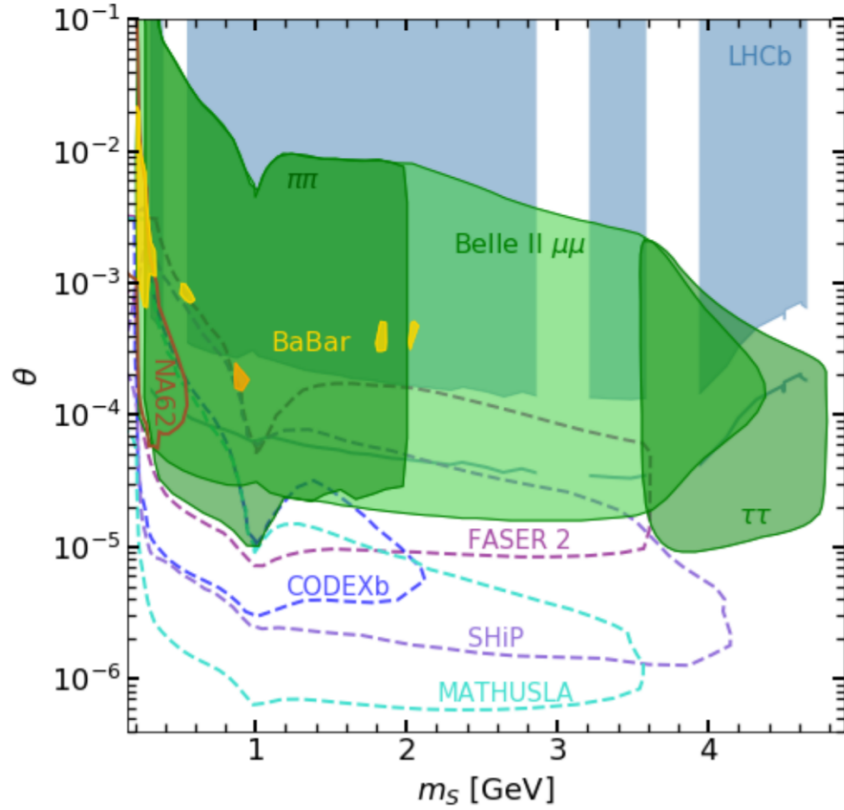


FIGURE 1.3: Searches for dark scalars with displaced vertices. The 95% CL bounds from $B^+ \rightarrow K^+ S(\rightarrow \mu^+ \mu^-)$ searches at LHCb are shown in blue. The yellow and orange show 90% CL bounds from the inclusive $B \rightarrow X_s S(\rightarrow f)$ where $f = \mu^+ \mu^-$ and $f = \pi^+ \pi^-$ respectively. Regions of 3σ significance at Belle II are shown in green for $B \rightarrow KS(\rightarrow f)$, where f is indicated on the figure. Predictions for proposed experiments are also shown.

1.2.5 Summary of previous searches

Experiment (Year)	Mass range (GeV/c^2)	Lifetime range	Channel
Belle (2010)	0.212 - 0.300	Up to $c\tau = 3 \times 10^{-8}$ cm	$B^0 \rightarrow K^{*0} X(\rightarrow \mu^+ \mu^-)$ $B^0 \rightarrow \rho^0 X(\rightarrow \mu^+ \mu^-)$
Belle (2013)	0.5 - 5.0	Up to $c\tau = 20$ m	$B \rightarrow X \ell \nu_h$
BaBar (2015)	0.5 - 9.5	$1 \text{ cm} < c\tau < 50 \text{ cm}$	$B \rightarrow X_s L$
LHCb	0.25 - 4.7	$0.003 \text{ cm} < c\tau < 30 \text{ cm}$	$B^+ \rightarrow K^+ \chi(\rightarrow \mu^+ \mu^-)$
CHARM	0.003 - 1	Up to 0.037 s	$x^0 \rightarrow \ell^+ \ell^-$

TABLE 1.1: A summary of the past searches for long-lived particles we have presented in this chapter. In the 2013 Belle study, the lifetime of 2000 cm is what is predicted by theory for the heavy neutrino ν_h . A partial reconstruction technique was used in order to improve efficiency, however 20 m is still a very optimistic lifetime to probe in the Belle detector.

1.3 The role and scope of this analysis

In this thesis, we lay the groundwork for a search for long-lived particles at Belle II. By creating a set of selection criteria that can be used to find events containing long-lived particles, we demonstrate what kind of background levels to expect when conducting a new particle search. Furthermore, we offer the first measurement of displaced track finding efficiency at Belle II using real data.

It should be noted that the specific model or process is not the main interest of this work; more generally, we are interested in how sensitive the Belle II experiment is to event topologies containing long-lived particles, and how one might go about constructing a search for scalars using their displaced decay products. We use a number of models to motivate our work, and show how results from detector performance studies can be applied to them.

To begin, we generate our own signal Monte Carlo (MC) samples and to investigate how new long-lived particles would interact with the detector. MC generation uses repeated random sampling based on interactions between particles and detector components to obtain a simulated dataset. The model used for MC generation can be tweaked to include non-SM particles such as our new long-lived scalar S , with freedom to choose its mass and lifetime.

In Chapter 3, we use the signal MC sample to demonstrate what various signals would look like in the detector, and show for what ranges of mass and lifetime a long-lived particle will actually decay in the detector volume. In Chapter 4, we design a set of selection criteria used to reconstruct signal decay channels for two different models and set upper limits on the number of background events we would expect in a search using one of these modes.

It is of great importance to understand how efficiently a detector can find tracks that originate far from the IP in a search for a long-lived particle. To do this, we use a partial reconstruction technique developed for B factories to measure tracking efficiency for the first time in the Belle II experiment. Furthermore, we extend this technique to study the track finding efficiency of highly displaced tracks for the first time. The results of this study are presented in Chapter 5, based on nearly 9fb^{-1} of data from the Belle II detector.

Finally, the results of the work in Chapters 4 and 5 are combined in Chapter 6 to give the most up-to-date estimate of the Belle II detector's sensitivity to long-lived particles, with results presented in reference to the branching fraction of a specific decay channel containing a dark scalar produced through a Higgs-like coupling.

Chapter 2

The Belle II Experiment

As the field of particle physics evolves, it continues to push new experimental frontiers in order to probe the fundamental laws of nature ever more precisely. Modern collider experiments continue to push boundaries on two frontiers; colliding particles at higher energies (the ‘energy frontier’), and colliding greater numbers of particles together (the ‘intensity frontier’). Belle II is at the forefront of the intensity frontier. It has a target dataset 50 ab^{-1} , more than fifty times larger than the total time integrated luminosity of its predecessor Belle, which collected 988 fb^{-1} . With this massive dataset, Belle II will provide the most precise measurements on a number of new physics searches [23].

2.1 The SuperKEKB Collider

The SuperKEKB collider is a next generation e^+e^- collider designed to achieve a record-breaking instantaneous luminosity of $8 \times 10^{35} \text{ cm}^{-2}\text{s}^{-1}$. The key to reaching this luminosity was squeezing the electron/positron beam size at the collision point so that the area over which the beams crossed was reduced, leading to a higher density of particles in the interaction region. Using what is known as a ‘nano-beam’ scheme (invented for the now-scraped Italian super B factory), the beam size was reduced to 50 nm at the collision point. Asymmetric beam energies of 7 GeV for electrons and 4 GeV for positrons provide a boost to the centre-of-mass system which allow for studies of time-dependent charge-parity violation. The centre-of-mass energy the collider operates at is just above that of the $\Upsilon(4S)$ resonance, at 10.58 GeV, which is slightly greater than twice the mass of a B meson. This allows large numbers of B meson pairs to be produced.

On June 15 this year, SuperKEKB reclaimed the instantaneous luminosity record from the LHC, surpassing their record of $2.14 \times 10^{34} \text{ cm}^{-2}\text{s}^{-1}$. Within a few days, SuperKEKB delivered $2.40 \times 10^{34} \text{ cm}^{-2}\text{s}^{-1}$, which, as of November this year, is the highest instantaneous luminosity ever achieved.

2.2 Belle II Detector Components

The Belle II detector brings together measurements from a number of different components to reconstruct events from SuperKEKB’s collisions. In order to operate as a competitive modern B factory, it has excellent vertex ($\approx 50\mu\text{m}$) and momentum (up to momenta of $\approx 8 \text{ GeV}/c$) resolution,

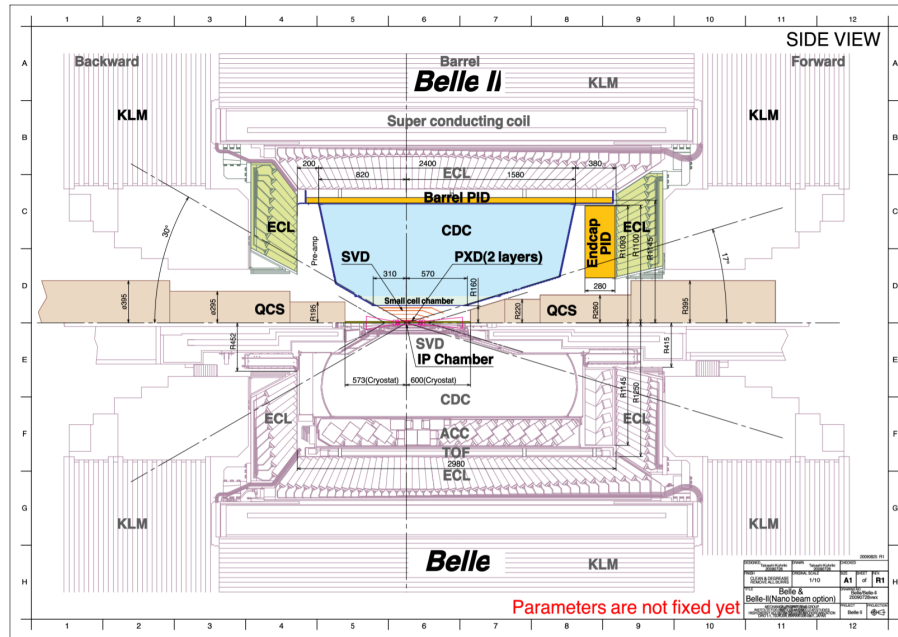


FIGURE 2.1: Cross-sectional layout of the Belle II detector (top half of image), illustrating relative size and placements of various subdetectors. The original Belle detector is illustrated in the bottom half as a comparison. The detector is described in cylindrical coordinates, with the z -axis going from left to right of this figure. The polar angle θ is measured anti-clockwise from the positive z -axis.

as well as very efficient reconstruction and identification of charged particles to separate electrons, muons, pions, kaons, protons and neutrons over the full kinematic range of the experiment.

2.2.1 Vertex Detector (VXD)

The innermost part of the Belle II detector is vertex detector, which comprises of two parts, the Pixel Detector (PXD) and Silicon Vertex Detector (SVD). These extend to a radius of 140 mm from the interaction point (IP), and offer a significant improvement on the vertex resolution compared to Belle. This provides a much better reconstruction efficiency for particles that decay in the VXD, such as $K_S^0 \rightarrow \pi^+\pi^-$. The polar angle acceptance of the SVD goes from 17° to 150° , with the asymmetry to account for the forward-boosted CMS frame due to asymmetric beam energies.

2.2.2 Central Drift Chamber (CDC)

The Central Drift Chamber extends out to a radius of 1130 mm, and has a large volume containing small drift cells filled with a He-C₂H₆ 50:50 mixture. The data from the CDC combines information from multiple layers of cells in different orientations to reconstruct 3D helix tracks of charged particles. This allows for the measurement of particle momentum and ionisation energy, which is important not only for event kinematics but for particle identification, as the energy deposited at different distances in the CDC changes depending on the mass of the particle. Tracking information from the CDC is the main input to Belle II's tracking algorithm, which is discussed in more detail in Chapter 5.

2.2.3 Particle identification system (TOP and ARICH)

The main subdetectors for particle identification at Belle II are the time-of-propagation (TOP) detector, located in the barrel region, and the aerogel ring-imaging Cherenkov counter (ARICH), located in the endcap region. The TOP detector measures the time of propagation of Cherenkov photons that are reflected internally inside a quartz crystal. An image of the Cherenkov ring is reconstructed from two spatial coordinates within the crystal, along with very precise timing. The ARICH detector allows Cherenkov photons to form rings on a photon detector surface, allowing for powerful separation between pions and kaons in the momentum range $0.4 \text{ GeV}/c$ to $4 \text{ GeV}/c$. Furthermore, it provides discrimination between electrons, muons and pions below $1 \text{ GeV}/c$.

2.2.4 Electromagnetic Calorimeter (ECL)

The ECL collects energy deposited by both electrically charged and neutral particles. It consists of a 3m long barrel with endcaps at $z = 1.96 \text{ m}$ and $z = -1.02 \text{ m}$ in the forward and backward regions respectively. It covers the polar angle region $12.4^\circ < \theta < 155.1^\circ$, with small gaps between the barrel and endcaps. The barrel contains 6624 truncated pyramid-shaped CsI(Tl) crystals, each being 30 cm or $16.1X_0$ long, where X_0 is the mean distance over which a high-energy electron loses energy by a factor of e . There are 2112 CsI crystals in the endcaps, for a total of 8736 crystals with a mass of 43 tons. Information from the electromagnetic calorimeter allows us to distinguish between electrons and hadrons (particularly pions).

2.2.5 K_L^0 - Muon Detector (KLM)

The K_L^0 and muon detector (KLM) is the outermost layer of the Belle II detector, located outside of the superconducting solenoid. It consists of alternating 4.7 cm thick iron plates and active detectors. The iron provides substantially more interaction length per centimetre than any of the previous detectors, which means K_L^0 mesons are much more likely to shower hadronically in the KLM. Unlike electron and pions, most muons can travel all the way through the ECL, and so a track left by a charged particle in the CDC with a corresponding hit in the KLM is most likely a muon. The KLM is arranged in an octagonal barrel with endcaps that in total cover a polar angle range of $45^\circ < \theta < 125^\circ$. There are 15 detector layers in the barrel and 14 in the endcap, and 14 iron plate layers in both. The detector modules are resistive plate chambers (RPCs), which consist of layers of glass electrodes with gas in between them. When a charged particle ionises the gas molecules along its path. Charged particles from this ionisation then drift towards the electrodes, leading to a pulse that is imaged on a plane of external pickup strips.

Muon identification starts with the reconstruction of a charged track in CDC. The track is extrapolated out to a larger radius. If the track is within the KLM acceptance and a hit in the KLM is found near the expected crossing of the extrapolated track, that hit is then associated with the track. The muon detection efficiency is 89% above momenta of $1 \text{ GeV}/c$.

2.2.6 Trigger system

The Belle II trigger system plays an important role in identifying interesting events during data taking. It consists of two levels: the hardware based low level trigger L1, and the high level trigger (HLT) which is based on software. Combined, these triggers reduce the event rate to 10 kHz from

Events with B - and D -decays are identified (with an efficiency of close to 100%) from the presence of at least 3 tracks in the CDC and a large amount of energy deposited in the ECL. There are also triggers for other event topologies that might be of interest, for instance single-photon triggers for dark sector searches.

2.2.7 Charged particle identification variables

Each subdetector provides a likelihood for each of the six possible long-lived charged particles. The available likelihoods are combined to form PID variables such as muonID. The likelihood that a candidate is a muon is given by the likelihood it is a muon divided by the sum of all likelihoods

$$\mathcal{L}_\mu = \frac{\sum_i \mathcal{L}_{i,\mu}}{\sum_j (\sum_i \mathcal{L}_{i,j})}. \quad (2.1)$$

where $j \in e, \mu, \pi, K, p, d$ and likelihoods are summed over each subdetector i . Not all charged particles have hits in all detectors as they could come from decays of long-lived neutral particles that leave no trace in the detector before they decay. For particles where no identification can be done, the value of all of its PID variables will be $1/6$.

2.3 Vertex Fitting

Vertex fitting is another key component of modern experimental particle and nuclear physics. It allows physicists to extract precise information about particles' decay vertices, while simultaneously suppressing combinatorial background and improving momentum resolution.

Since at least the mid 1970s, vertex fitting has been implemented at high energy physics experiments. At CERN's Split Field Magnet Detector (SFMD), vertex fits were performed on single reconstructed tracks, first for decay topologies with only two charged particles, and later extended for higher multiplicity events [24]. Here, the trajectory of a particle was defined by five independent parameters (p_1, \dots, p_5) , just as tracks are defined at Belle II. In the SFMD, multiwire proportional chambers measured particle trajectories. In general, vertex fitting uses a least squares fit procedure to find the most likely vertex coordinate. Once the track parameters have been calculated, a common vertex needs to be fitted. At the same time, a the momenta is fitted using the vertex as a constraint.

2.3.1 Global decay chain vertex fitting

The parameterisation of an entire decay chain in terms of the vertex coordinates, momenta and decay times is known as a global decay chain fit. By extracting the relevant parameters of a reconstructed final state particles and using intermediate particles to reconstruct other 'upstream' decays, a global fit can be obtained. At the BaBar experiment, a global vertex fitting technique was developed that employed a Kalman filter to minimise the χ^2 of the vertex fit for the first time [25] (although using a Kalman filter for vertex fitting had been considered in the past [26]).

The global decay chain fit used at BaBar was used in a number of different analyses. It proved to be an improvement of previous leaf-by-leaf fitting techniques, especially for decay chains with poorly constrained intermediate vertices, such as $\Xi^0 \rightarrow \Lambda^0 \pi^0$ and $K_S^0 \rightarrow \pi^0 \pi^0$.

2.3.2 Tree Fitter

The Belle II experiment has its own global decay chain vertex fitter, Tree Fitter [27]. The decay chain is parameterised in a way that reduces the dimensionality of the problem; e.g for final state particles, only the momenta are saved, as we have no interest in their decay vertices.

Particles that decay via the strong force with a lifetime of less than 10^{-14} s are treated as if the decay instantly, as their boosted flight lengths in the detector would be of order $1 \mu\text{m}$, while the resolution of the vertex detector at Belle II is $20 - 30 \mu\text{m}$ in the plane transverse to the beam direction. Weakly decaying particles are longer-lived, and so a decay vertex is measured, as well as a flight length, defined as the 3D distance between the production vertex and decay vertex. Photon vertex parameters can be inferred using the position of the calorimeter cluster they produce.

2.3.3 Constraining a decay chain

There are a number of constraints that can be applied to a decay chain. A kinematic constraint ensures that 4-momentum is conserved at a vertex, so the four-momenta sum of the daughter particles is the four-momentum of the mother. Another method is the geometric constraint, which uses the decay length parameter θ (the magnitude of the distance between the production and decay vertex), and the flight vector $\mathbf{\Delta} = \theta \cdot \mathbf{p}/|\mathbf{p}|$. The constraint itself is that the vertex of the mother and the daughter minus its flight path are the same

$$0 = \mathbf{u}_{mother} + \mathbf{\Delta} - \mathbf{u}. \quad (2.2)$$

The mass constraint uses the nominal mass of the particle reported by the Particle Data Group (PDG) [28]. The particle's four-vector must be consistent with the nominal mass.

The beam spot constraint limits the production vertex of all e^+e^- daughters to an area within the three dimensional uncertainty of the beam spot region. This region is determined by averaging the coordinates of the e^+e^- collisions over a large number of collisions.

A particularly useful constraint when dealing with decay chains containing particles that cannot be detected (such as neutrinos or long-lived scalars/dark matter particles) is a custom origin constraint, which is another geometric constraint. It is created by defining a vertex position and an uncertainty to be the origin of the decay chain. For example, if one knows the particle originates from a B meson, the average B decay vertex could be used. It isn't useful to fit the full decay chain as it renders the kinematic constraint on the mother particle incorrect. When using this constraint, the beam energy constraint is not required as a mass constraint can be set on the $\Upsilon(4S)$.

Chapter 3

Monte Carlo simulation of long lived particles

Constructing a new physics analysis starts with simulating the new processes using Monte Carlo (MC) generation. Studying signal MC allows us to identify what a signal would look like at the Belle II detector in terms of detector hits and event kinematics, as well as give insight into our signal finding efficiency. Armed with the knowledge of how the new process looks in the detector, we can go forth and construct some selection criteria that select signal events and reject non-signal (background) processes.

3.1 MC Generation

Dark scalar MC events were generated using `evtgen` [29], a generator in the Belle II Software Analysis Framework (`basf2`) [30]. In the following section, decaying ‘generically’ refers to a simulated particle decaying according to its full set of measured branching fractions. In order to generate a long-lived particle without having to create one from scratch in `evtgen`, the mass and lifetime of an existing neutral particle with non-zero lifetime were altered so suit our needs. The interactions between particles in these events and the Belle II detector are simulated using `Geant4` [31].

We generate 10000 signal events for a number of mass ($m_S = 0.215, 0.5, 1, 2, 3, 4$ and $4.78 \text{ GeV}/c^2$) and lifetime ($c\tau_S = 10^{-3}, 10^{-1}, 1, 5, 10, 50$ and 100 cm) hypotheses for both the scalar channel $B^+ \rightarrow K^+ S (\rightarrow \mu^+ \mu^-)$ and the ALP channel $B^0 \rightarrow \bar{D}^0 a' (\rightarrow \mu^+ \mu^-)$. The generated events all start with an e^+e^- collision at the $\Upsilon(4S)$ resonance of 10.58 GeV , which then decays into a $B\bar{B}$ pair. One of the B mesons decays generically while the other (which we call B_{sig}) decays via one of the signal channels. The K/D^0 daughter of B_{sig} decays generically. In half of the events generated, the charge conjugate of the signal channel occurs. For the rest of this work, the charge conjugate decays $B^- \rightarrow K^- S (\rightarrow \mu^+ \mu^-)$ and $\bar{B}^0 \rightarrow D^0 a' (\rightarrow \mu^+ \mu^-)$ are implied.

3.2 Dimuon kinematic distributions

The invariant mass distribution for dimuon background is shown with a number of overlaid signal MC samples for various masses of long-lived scalars. The combined invariant mass of the dimuon

system should be that of the generated scalar. Clearly, we see that the dimuon masses peaks at the generated scalar mass in Figure 3.1. The dimuon invariant mass cuts off at $2m_\mu \approx 210\text{MeV}$. Here, we chose to show distributions where the generated signal channel is $B^0 \rightarrow \bar{D}^0 S(\rightarrow \mu^+ \mu^-)$.

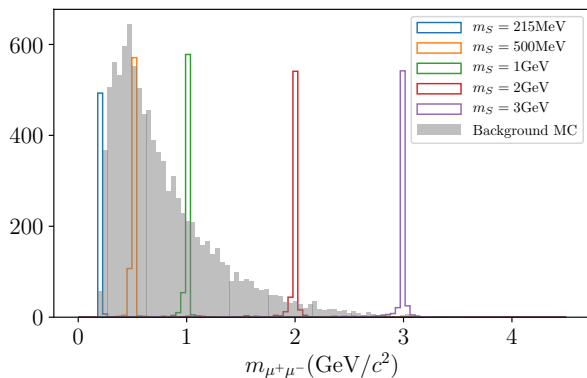


FIGURE 3.1: Invariant mass of final state muons for different mass hypotheses, with background overlaid in grey. The greatest amount of background is in the region below 1 GeV, with a cutoff at twice the muon mass.

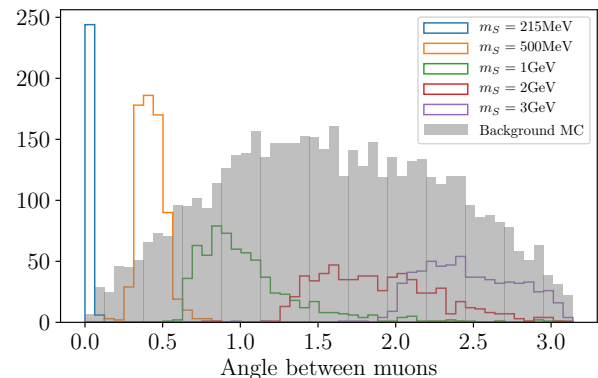


FIGURE 3.2: Lab frame polar angle between final state muons for different mass hypotheses, with background overlaid in grey. Notice that for a smaller mass hypothesis, the angle between daughters is narrower.

We examine where the decay vertices for long-lived particles are for different lifetime hypotheses in Figures 3.3 and 3.4.

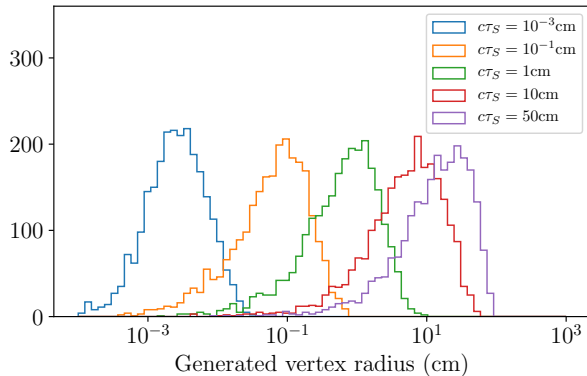


FIGURE 3.3: Histogram of generated vertex radii for a 2 GeV scalar. Here, we only kept events where the displaced muon pair was seeing in the detector. Belle II's tracking volume ends at a radius of about 1m, hence why the distribution for the $c\tau_S = 50\text{cm}$ case is somewhat cut off on the right hand side.

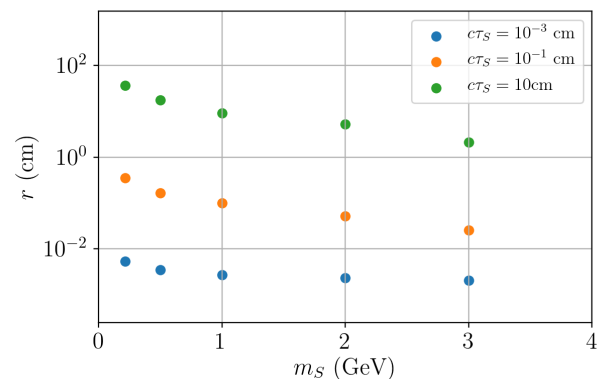


FIGURE 3.4: Median generated decay vertex radii for a selection of mass and lifetime hypotheses. For particles with the same lifetime hypothesis, we see more displaced vertex at lower masses.

3.3 Sensitivity to displaced decay products

Using generated quantities from MC for multiple mass and lifetime hypotheses for a long-lived scalar produced in the decay $B^+ \rightarrow K^+ S(\rightarrow \mu^+ \mu^-)$, we can see how likely it is for muon daughters to hit

various subdetectors. In general, lighter scalars are more boosted and travel further than a heavier scalar with the same lifetime, meaning that it is less likely for daughters from light long-lived scalars to hit inner detectors like the SVD. Obviously, the greater the lifetime of the scalar, the further it travels through the detector, so scalars with a smaller mixing angle θ produce more highly displaced daughters.

Mixing angle	0.215GeV	0.500GeV	1GeV	2GeV	3GeV
$\theta \approx 10^{-2}$	0.928	0.929	0.920	0.918	0.935
$\theta \approx 10^{-3}$	0.934	0.934	0.921	0.925	0.925
$\theta \approx 10^{-4}$	0.928	0.920	0.925	0.914	0.924

TABLE 3.1: Fraction of muons that have polar angle within CDC acceptance for five different mass hypotheses.

Mixing angle	0.215GeV	0.500GeV	1GeV	2GeV	3GeV
$\theta \approx 10^{-2}$	0.935	0.937	0.924	0.924	0.942
$\theta \approx 10^{-3}$	0.937	0.941	0.929	0.934	0.929
$\theta \approx 10^{-4}$	0.202	0.372	0.575	0.780	0.939

TABLE 3.2: Fraction of muons that are seen in the SVD for five different mass hypotheses.

Mixing angle	0.215GeV	0.500GeV	1GeV	2GeV	3GeV
$\theta \approx 10^{-2}$	0.958	0.958	0.950	0.950	0.961
$\theta \approx 10^{-3}$	0.956	0.961	0.955	0.951	0.951
$\theta \approx 10^{-4}$	0.780	0.901	0.931	0.936	0.935

TABLE 3.3: Fraction of muons that are seen in the CDC for five different mass hypotheses.

Chapter 4

Preparing a search for new long-lived particles

So far we have shown what events containing long-lived particles would look like in the detector, however we have not explored how a specific channel containing a new long-lived particle would be reconstructed. To construct a search for a new particle, we must be able to discriminate between signal and background events, and so in this chapter we examine two possible channels in which we could find a new long-lived particle S , and show to what extent background events could be rejected. The first channel we consider here is the Higgs-like production detailed in Section 1.1.1, $B^+ \rightarrow K^+ S (\rightarrow \mu^+ \mu^-)$. We also consider a channel where a long-lived particle a' is produced as an ALP, detailed in Section 1.1.2. For both of these modes, we construct a set of selection criteria for reconstructing the decay chain containing S . The signal MC used to construct this analysis uses a long lived particle with mass $2 \text{ GeV}/c^2$ and lifetime $c\tau = 10 \text{ cm}$.

4.1 Background processes

In previous searches for long-lived particles, dominant sources of peaking background included hadronic events from which highly displaced tracks could originate. Decays such as $K_S^0 \rightarrow \pi^+ \pi^-$ and $\Lambda^0 \rightarrow p^+ \pi^-$ were the biggest sources of these peaking backgrounds. K^\pm and π^\pm may also travel some distance through the detector and produce displaced tracks, however they will never produce only two charged daughters, and so this component of the background will not peak. Deep inelastic scattering of produced leptons with baryons in detector material can produce hadronic resonances which decay into tracks. In the BaBar study referenced earlier [16], random overlaps of tracks produced in this way produced most of the background candidates. Finally, electromagnetic interactions between photons and atoms in the detector material can lead to electron pair production. We can clearly see how many tracks are created by interactions with the detector material by looking at the production vertex coordinates of MC truth-matched electrons in Figure 4.1.

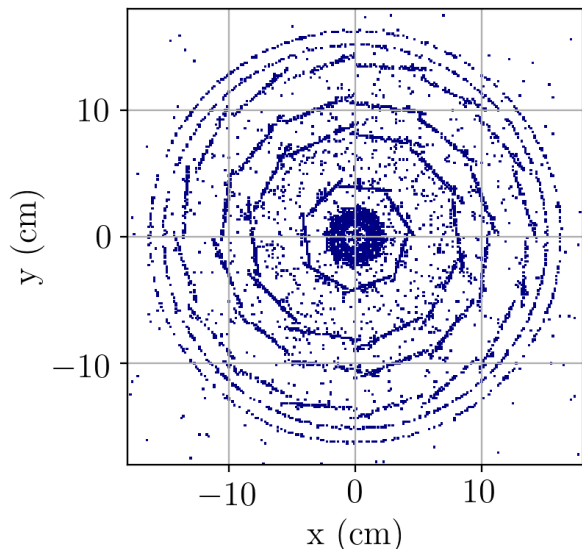


FIGURE 4.1: Generated production vertex coordinates of true electrons in the radial plane.

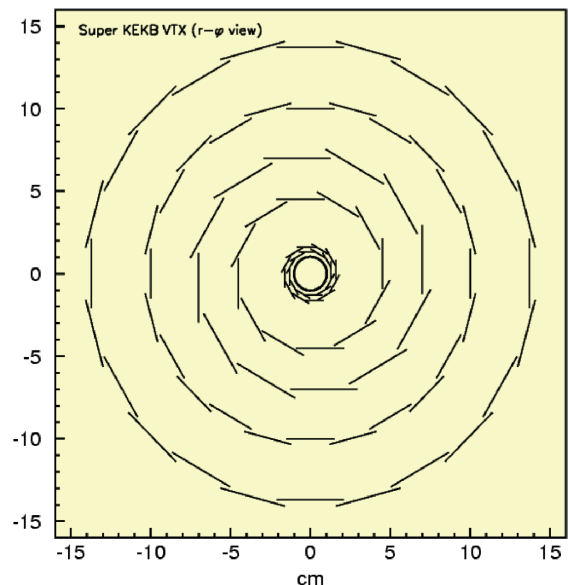


FIGURE 4.2: VXD layout in the Belle II detector in the radial plane.

4.2 Higgs-like channel

4.2.1 Reconstruction

Reconstruction is done in `basf2` with the preselection criteria in Table 4.1 on a sample of 10,000 signal events, 10 fb^{-1} of $q\bar{q}$ ($q = u, d, s, c$) events, and 10 fb^{-1} of B^+B^- and $B^0\bar{B}^0$ events.

Criteria	Description
<code>muonID > 0.6</code>	well-identified muons
<code>kaonID > 0.6</code>	well-identified charged kaons
$dr(K^\pm) < 0.5 \text{ cm}$ and $dz(K^\pm) < 2 \text{ cm}$	kaons originate near IP
$B_{sig}^+ M_{BC} > 5.24 \text{ GeV}/c^2$	signal-side beam energy constrained mass
$B_{sig}^+ \Delta E < 0.2 \text{ GeV}$	signal-side ΔE cut

TABLE 4.1: Higgs-like channel preselection criteria.

To reconstruct the decay, a pair of muons are combined to form an S . We require that muons are ‘well-identified’ to reject tracks caused by other particles such as electrons or pions. This cut alone removes just over 92% of tracks that are true electrons. A well-defined K^\pm that originated from near the IP is then added to the scalar to build the B^\pm candidate. A global decay chain vertex fit is performed with `TreeFitter` using the K^+ mass to constrain the fit. The candidate is kept if it satisfies beam energy constrain mass (M_{BC}) and difference between reconstructed and expected energy ($|\Delta E|$) cuts. M_{BC} and ΔE are given by the following:

$$M_{BC} = \sqrt{\frac{E_{\text{beam}}^{*2}}{c^4} - \frac{\vec{p}_B^{*2}}{c^2}}, \quad (4.1)$$

$$\Delta E = E_B^* - E_{\text{beam}}^*. \quad (4.2)$$

Selection criteria are tightened on M_{BC} and $|\Delta E|$, and new criteria are introduced after the initial processing in `basf2`. We require that the radial vertex coordinate of S is at least 0.4 cm from the IP to remove backgrounds from prompt decays. The majority of background events that contain a displaced vertex comes from K_S^0 decays, most of which are $K_S^0 \rightarrow \pi^+\pi^-$ where the pions have made it past the muon selection criteria. To veto these, we reconstruct the S candidate from tracks given a pion mass hypothesis (rather than a muon mass hypothesis) and recalculate the invariant mass. Any candidates with invariant mass from the alternative hypothesis within 50 MeV of the nominal K_S^0 mass of 497 MeV/ c^2 are removed. The same is also done for the $\Lambda^0 \rightarrow p^+\pi^-$ channel and electron pair production $\gamma \rightarrow e^+e^-$. The mass distributions of these peaking backgrounds is shown in Figure 4.3.

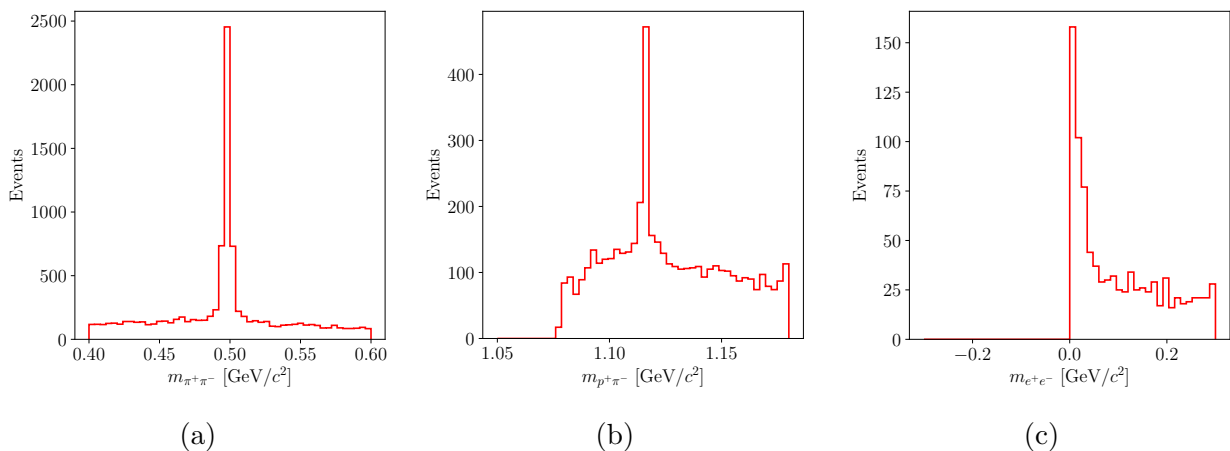


FIGURE 4.3: Invariant mass of peaking backgrounds coming from decay channels $K_S^0 \rightarrow \pi^+\pi^-$ (a), $\Lambda^0 \rightarrow p^+\pi^-$ (b) and $\gamma \rightarrow e^+e^-$ (c), calculated with daughter mass hypotheses pertaining to the channel rather than the muon mass hypothesis.

We also require that the vertex fit p-value is greater than 0, meaning that the vertex fit must have succeeded, however we do not cut out events with vertex fits that may be of poor quality. The angle between the momentum and vertex vectors of the scalar candidate θ must also be very small. We transform this angle using

$$\theta' = \log_{10}(1 - \cos(\theta)) \quad (4.3)$$

and require that $\theta' < -1$. Finally, we can use two-body decay kinematics to perform cuts. The momenta of two particles (with masses m_1 and m_2) produced in a two-body decay in the frame of their mother particle (with mass M) are equal and opposite, and given by

$$|p_1| = |p_2| = \frac{\sqrt{[M^2 - (m_1 + m_2)^2][M^2 - (m_1 - m_2)^2]}}{2M}. \quad (4.4)$$

We can eliminate a lot of background by requiring the K^+ meson's B -frame momentum be within 50 MeV/ c of the momentum predicted by the mass hypothesis m_S and Equation 4.4.

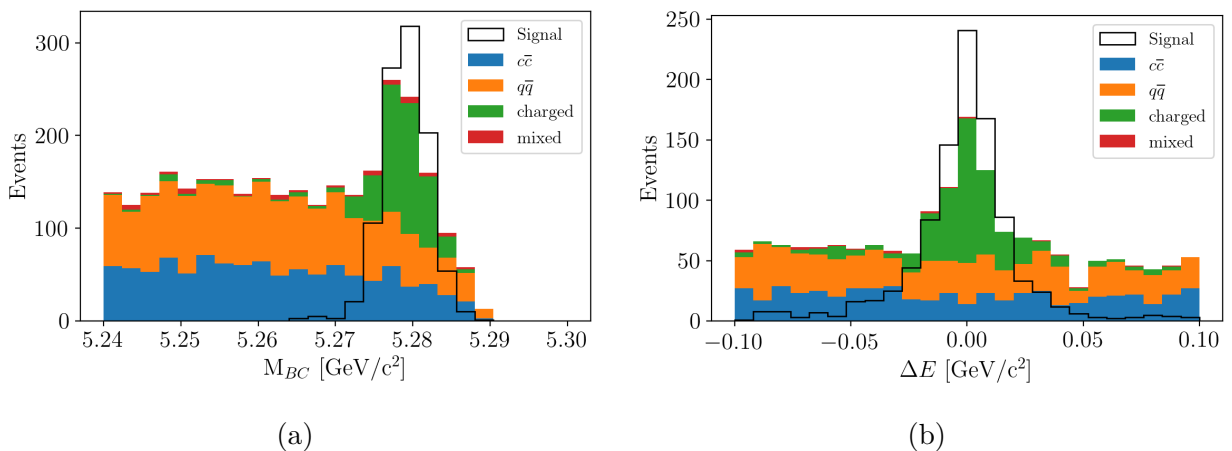


FIGURE 4.4: Distributions of M_{BC} (a) and ΔE (b) for all candidates after preselection criteria for signal and background MC. Note that the overlaid signal distribution is arbitrarily scaled.

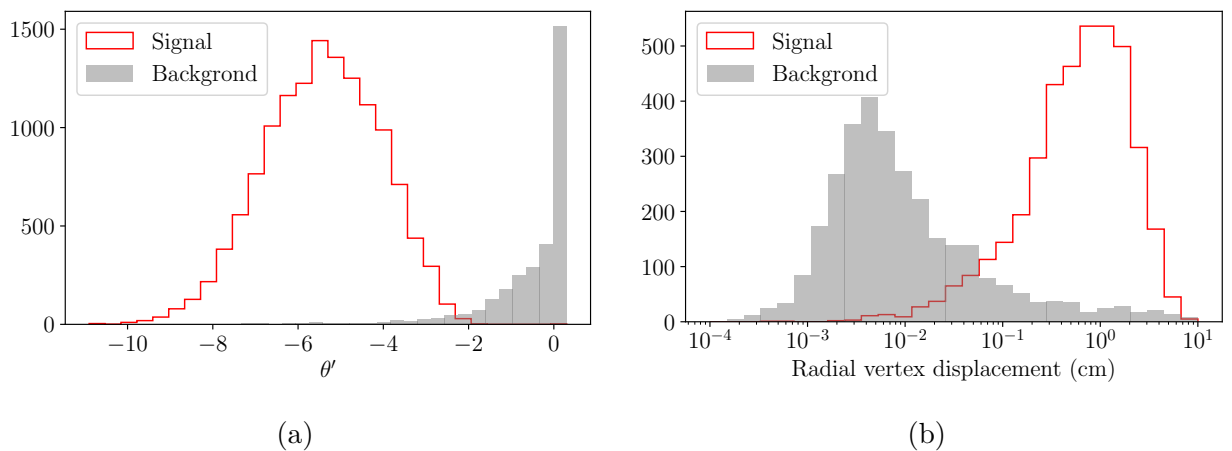


FIGURE 4.5: (Signal and background distributions of θ' (a) and the scalar decay vertex radial displacement (b).

4.2.2 Higgs-like channel efficiency

With our full set of selection criteria we can set an upper limit on the number of background events of one event per 10 fb^{-1} , while maintaining a signal reconstruction efficiency of 34.6%. The number of background events kept and signal efficiency for each cut in sequence is given in Table 4.2. The efficiency for each of these cuts applied one at a time is also shown in Table 4.2. The criteria rejected all of the events in the sample processed, and so the true number of background events per fb^{-1} could be much lower.

Criteria	Signal eff	Signal eff. in sequence	Neutral	Charged	$q\bar{q}$	cc	All
Preselection	0.442	0.442	66	502	1455	1100	3123
K_S^0 veto	0.442	0.442	65	500	1368	1049	2982
γ veto	0.442	0.442	65	500	1367	1046	2978
Λ^0 veto	0.442	0.442	64	498	1348	1032	2942
$M_{bc} > 5.27 \text{ GeV}/c^2$	0.437	0.437	30	455	376	296	1157
$ \Delta E < 0.05 \text{ GeV}$	0.397	0.396	2	379	85	71	537
$dr(S) > 0.4 \text{ cm}$	0.416	0.374	0	0	5	2	7
Vertex p-value > 0	0.429	0.370	0	0	0	1	1
$\theta' < -1$	0.438	0.370	0	0	0	1	1
$2.18\text{GeV}/c < p_{K^+}^{B\text{frame}} < 2.28\text{GeV}/c$	0.414	0.346	0	0	0	0	0

TABLE 4.2: Signal efficiency after preselection and single cut (first column), as well as signal efficiency and number of background events kept when the cuts are applied in sequence.

$m_S \text{ (GeV}/c^2)$	Signal efficiency after all selection criteria are applied
0.215	0.04 ± 0.006
0.500	0.368 ± 0.019
1.0	0.347 ± 0.019
2.0	0.346 ± 0.019
3.0	0.46 ± 0.021
4.0	0.45 ± 0.021
4.78	0.06 ± 0.008

TABLE 4.3: Signal reconstruction efficiency for a number of mass hypotheses for S , all with a lifetime $c\tau = 10 \text{ cm}$.

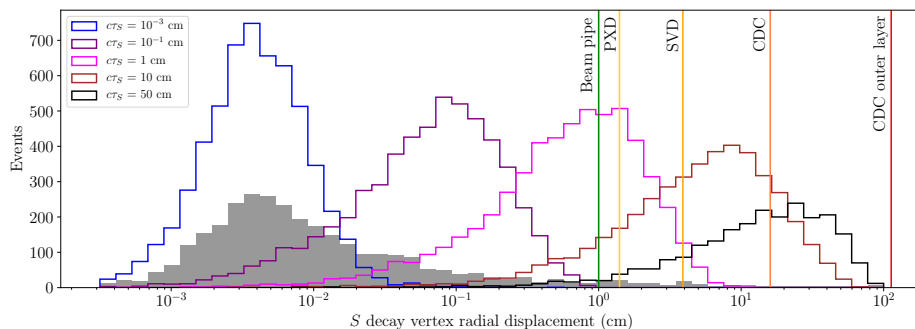


FIGURE 4.6: Radial displacement of a $2 \text{ GeV}/c^2$ scalar's decay vertex for different lifetime hypotheses. Combinatorial background after preselection criteria is overlaid in grey. Very few background events with radial vertex displacements greater than 1mm survive the preselection criteria. Vertical line indicate the approximate radius of various subdetectors to contextualise the distances presented.

4.3 ALP channel

The D^0 meson in the ALP channel makes the reconstruction slightly more complicated than in the Higgs-like channel. The D^0 is reconstructed from three decay modes (listed in Table 4.4). The account for nearly 27% of the total D^0 decay width.

Decay channel	Fraction(Γ_i/Γ)
$D^0 \rightarrow K^- \pi^+$	$(3.950 \pm 0.031)\%$
$D^0 \rightarrow K^- \pi^+ \pi^0$	$(14.4 \pm 0.5)\%$
$D^0 \rightarrow K^- \pi^+ \pi^+ \pi^-$	$(8.23 \pm 0.14)\%$
Total	26.61%

TABLE 4.4: The three decay modes used to reconstruct the D^0 in this analysis.

4.3.1 Selection criteria

We implement more preselection criteria here when reconstructing the D^0 . The final state particles must all originate within 0.5cm of the IP in the radial plane, and must not originate from more than 2cm away from the IP in the z -direction. Furthermore, the charged pions must have a pionID greater than 0.1, while kaons must have a kaonID greater than 0.6. This eliminates most of the tracks that don't come from pions or kaons. The neutral pion in the second decay channel is built using a photon pair with momentum greater than 200 MeV/ c and a mass within 20 MeV/ c^2 of the nominal π^0 mass. Finally, the reconstructed D^0 must have a mass within 100 MeV/ c^2 of the nominal D^0 mass and momentum greater than 1 GeV/ c in the CMS frame. These criteria are fairly standard cuts used in analyses with a D^0 in Belle II.

Criteria	Description
muonID > 0.6	well-identified muons
pionID > 0.1	well-defined charged pions
$dr(\pi^\pm) < 0.5$ and $dz(\pi^\pm) < 2$ (cm)	pions originate near IP
kaonID > 0.6	well-defined charged kaons
$dr(K^\pm) < 0.5$ and $dz(K^\pm) < 2$ (cm)	kaons originate near IP
$p_{\pi^0} > 200$ (MeV/ c)	remove slow pions
$0.114 < m_{\pi^0} < 0.154$ (GeV/ c^2)	π^0 are near π^0 invariant mass
$1.764 < m_{D^0} < 1.964$ (GeV/ c^2)	$m_{K\pi}$ is near the D^0 invariant mass
$p_{D^0}^{CMS} > 1.0$ (GeV/ c)	D^0 CMS momentum cut
$B_{sig}^0 M_{BC} > 5.24$ (5.21) (GeV)	signal-side beam constrained mass
$B_{sig}^0 \Delta E < 0.2$	signal-side ΔE cut

TABLE 4.5: ALP channel preselection criteria.

4.3.2 ALP channel efficiency

The signal reconstruction efficiency is an order of magnitude lower than that of the Higgs-like mode, however the upper limit on number of background events is the same. In 10fb^{-1} , no background events make it through the selection criteria. While this is a relatively small sample, we expect to have very little to zero background after all criteria are applied even with a larger dataset.

Cuts	Signal eff.	Signal eff. in sequence	Neutral	Charged	$q\bar{q}$	cc	All
Preselection	0.067	0.067	13669	19803	21202	34105	88779
K_S^0 veto	0.067	0.067	13397	19395	19915	31534	84241
γ veto	0.067	0.067	13388	19387	19849	31459	84083
Λ^0 veto	0.067	0.067	13238	19095	19366	30268	81967
$M_{BC} > 5.27\text{GeV}$	0.066	0.066	4363	6345	5322	8536	24566
$ \Delta E < 0.05\text{GeV}$	0.061	0.060	1133	1433	1232	2001	5799
$dr(a') > 0.4\text{cm}$	0.062	0.056	76	133	94	198	501
Successful vertex fit	0.062	0.054	17	16	13	28	74
$\theta' < -1$	0.066	0.054	3	12	11	23	49
$2.18\text{GeV}/c < p_{K^+}^{B\text{frame}} < 2.28\text{GeV}/c$	0.057	0.046	0	0	0	0	0

TABLE 4.6: Signal efficiency after preselection and single cut (first column), as well as signal efficiency and number of background events kept when the cuts are applied in sequence for the channel $B^0 \rightarrow \bar{D}^0 a' (\rightarrow \mu^+ \mu^-)$

The signal reconstruction efficiency for the channel with \bar{D}^0 is lower than the K^+ mode by about a factor of 6-7, however it could be increased by substantially by reconstructing more D^0 decay modes.

4.4 Vertex fitting resolution on long-lived particles

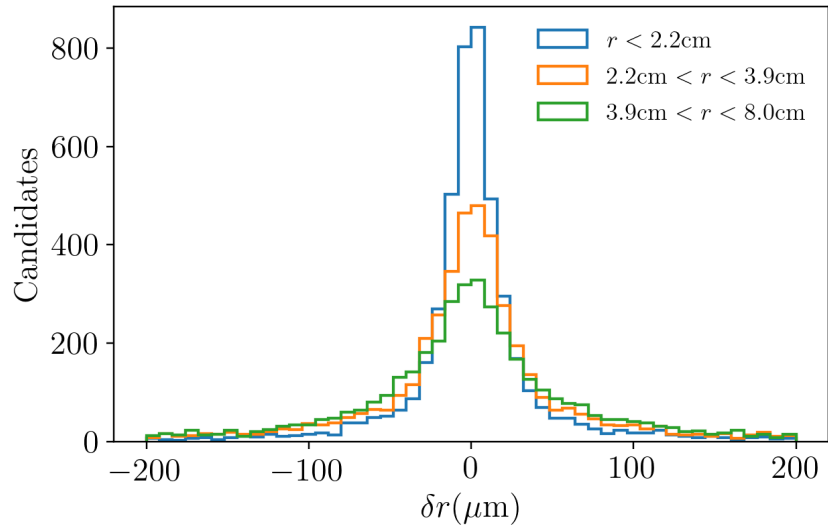
The Belle II tracking system is designed to track particles that are produced close to the interaction point, and so the nominal vertex detector resolution of 20-30 μm in the radial plane does not apply to vertices that have significant displacements. We expect resolution to decrease substantially if a particle decays beyond the VXD. TreeFitter is the vertex-fitting algorithm used here.

Using the signal MC generated for the Higgs-like mode, we studied the vertex resolution for displaced vertices at different detector radii corresponding to layers of the VXD. We define the resolution σ_{dr}^{68} as the 68th percentile range of distribution of the difference between generated and reconstructed vertices δr , using that same reconstruction method detailed in section 4.2. Candidates where the vertex fit failed were discarded. The decay chain was constrained using the K^+ mass during the vertex fit.

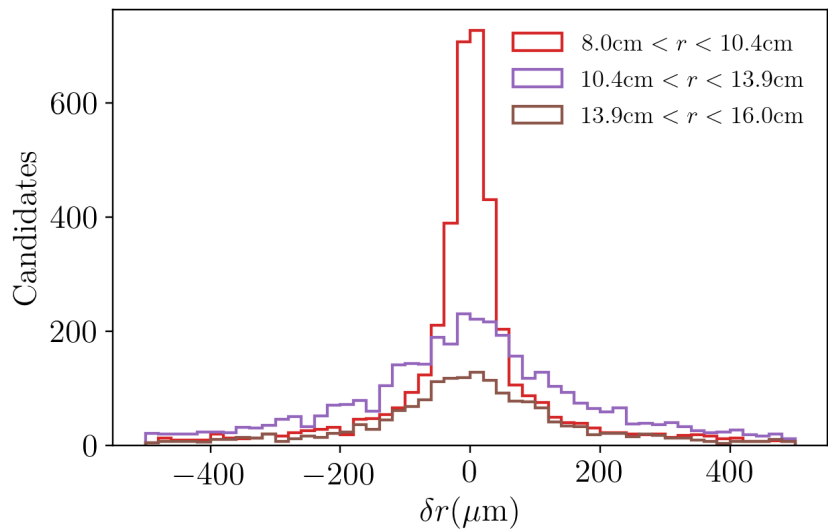
Vertex location	Detector radius	σ_{dr}^{68} (μm)
Before first PXD layer	$r < 2.2\text{cm}$	25.1
Between PXD layer 1 and 2	$2.2\text{cm} < r < 3.9\text{cm}$	58.6
Between PXD and SVD	$3.9\text{cm} < r < 8.0\text{cm}$	98.2
Between SVD layer 1 and 2	$8.0\text{cm} < r < 10.4\text{cm}$	119.9
Between SVD layer 2 and 3	$10.4\text{cm} < r < 13.9\text{cm}$	324.9
Between SVD and CDC	$13.9\text{cm} < r < 16.0\text{cm}$	288.2
Inner 10cm of CDC	$16.0\text{cm} < r < 26.0\text{cm}$	245.0
Inside CDC	$26.0\text{cm} < r < 36.0\text{cm}$	347.0
Inside CDC	$36.0\text{cm} < r < 46.0\text{cm}$	301.8
Inside CDC	$46.0\text{cm} < r < 56.0\text{cm}$	570.5
Outer region of CDC	$56.0\text{cm} < r < 113.0\text{cm}$	624.8

TABLE 4.7: Radial vertex resolution at different detector radii.

We find that the vertex resolution widens considerably as the vertex is further out from the interaction point, however the resolution remains less than 1mm even for vertices that are in the outer half of the CDC.



(a)



(b)

FIGURE 4.7: Distributions of σ_{dr}^{68} for the six innermost vertex regions from Table 4.7. Note the different scale on the horizontal axis between the two plots.

Chapter 5

Displaced track finding efficiency

Here we present the first ever tracking study at Belle II that measures the track finding efficiency of highly displaced tracks. The tracking hardware (discussed in Chapter 2) and algorithms at Belle II are designed primarily to find tracks that originate close to the interaction point, and looking for tracks that originate far beyond that push the detector towards its limits. For any studies of long-lived particles, it is important to know how efficiently the Belle II detector will find these particles' displaced charged decay products, and to see if there is any bias in the tracking system towards tracks that originate close to the IP. We use a partial reconstruction technique in order to estimate the efficiency. Measurements are taken with both MC and the data that Belle II collected in 2019.

5.1 Tracking at Belle II

Most tracks at Belle II originate from inside the beam pipe, with the exception of those originating from long-lived V^0 -like particles such as K_S^0 , Λ , and converted photons. V^0 particles in general refer to any long-lived neutral particles. A new long-lived scalar would also decay outside of the beam pipe, and so reconstructing events containing such particles would be very similar to reconstructing events with, for instance, a K_S^0 .

5.1.1 Charged particle reconstruction

The first step in reconstructing charged particles is finding a combination of detector hits that make a track. There are multiple algorithms used to do this; one for the VXD and two for the CDC. The VXD would produce 20 Gb/s of raw pixel data, and so background is cut out by the trigger system before data is written onto a disk [32]. The track finding algorithm first builds segments that connect two hits in adjacent layers of the VXD, then checks whether these segments satisfy various geometrical requirements. The algorithm is then iterated and track candidates are extracted from neighbouring segments.

The first algorithm the CDC uses is a global track finder [33]. It examines all hit positions simultaneously and looks for intersections between hits. It is very efficient in the high p_t region and can deal with tracks that have missing hits. The second algorithm is a local track finder that looks for hits with neighbouring hits in a similar manner to the VXD algorithm. The track candidates from both subdetectors are merged, with the combination providing excellent reconstruction efficiency.

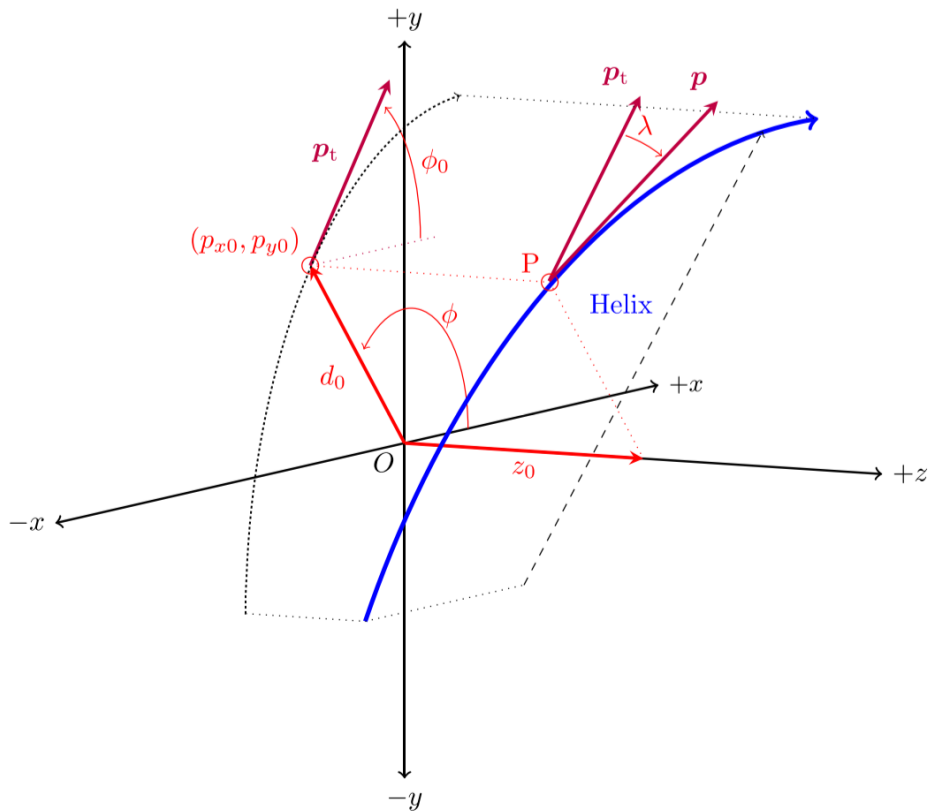


FIGURE 5.1: Parameterisation of a track helix (blue) with respect to P, the track's point of closest approach to origin. Diagram adapted from [27].

Using this tracking data, a fit needs to be done in order to reconstruct the track itself, and to find any relevant vertices. Track fitting requires a mass hypothesis so that the interaction of particles with matter can be correctly modelled. A charged particle moving in a vacuum in a constant magnetic field moves along a helix. At a point \vec{P} of the trajectory, the helix can be described by five parameters:

- d_0 : the signed distance of the perigee from the origin in the transverse plane. The sign depends on the direction of the angular momentum of the track at the perigee with respect to the magnetic field.
- z_0 : the longitudinal signed distance of the perigee from the origin.
- ϕ_0 : the angle between the transverse momentum at the perigee and the x axis.
- $\tan \lambda$: the tangent of the angle between the momentum at the perigee and the transverse plane.
- ω : the curvature. The sign corresponds to the charge of the track.

At Belle II, the helix is defined at the point of closest approach of the helix to the coordinate system's origin.

The real paths of particles at Belle II are not ideal helices as charged particles lose energy and undergo scattering in the material of the detector. Furthermore, the magnetic field is not constant. These factors are taken into consideration during track fitting.

5.1.2 V^0 -like particle reconstruction

Heavy, neutral, unstable subatomic particles or V^0 's that decay into a pair of charged particles at a point displaced from the IP are reconstructed with a different algorithm. After the charged particle reconstruction has taken place, the algorithm extrapolates the innermost hit of two oppositely charged tracks, for all combinations of oppositely charged tracks. If this fails, the track combination is rejected. The combinations that pass are processed by a vertex fitter that finds coordinate at which the V^0 decays. The candidates that survive the vertex fit can then be cut on using the vertex fit χ^2 and the mass (within 30 MeV/ c^2 of the nominal V^0 mass).

Searching for a dark scalar at Belle II, as well as any other new physics search containing displaced track vertices, requires an understanding of the relationship between track finding efficiency and their displacement in both data and MC. The track finding efficiency in both data and MC play an important role in these searches. Due to the geometry of the detector, a track that originates further away from the IP will generally cross less of the tracking volume than a track produced at the IP. A K_S^0 may travel all the way through the vertex detector and decay in the CDC, meaning that its daughters will not register hits on two whole subdetectors (PXD and SVD). However, it should be noted that not all neutral long-lived particles are V^0 's; decays with more than two tracks are possible.

5.2 Measuring track finding efficiency using partially reconstructed D^* decays

The uncertainty in track finding efficiency is a source of systematic error that needs to be further studied in Belle II. Track finding efficiency η_{Found} is essentially the ratio of number of tracks found to the total number of tracks produced. This presents us with an obvious problem: How do we know when we haven't found a track? Partially reconstructing decays provides us with an elegant solution. A decay chain can be reconstructed even with a missing track by inferring its existence through various kinematic constraints. The track finding efficiency is determined by the rate at which the non-used track was found.

It is important to understand the track finding efficiency and its associated systematic uncertainty for any physics analysis that uses a charged track in some way. In a search for a long-lived scalar, it is important to understand how tracking efficiency is related to the displacement of tracks. Partial reconstruction methods were used to estimate tracking efficiencies in the Belle experiment [34, 35]. Here, we adapt the methods used in Belle to Belle II for the first time.

The decay chain $D^{*+}(2010) \rightarrow \pi^+ D^0$, $D^0 \rightarrow \pi^+ \pi^- K_S^0$ and $K_S^0 \rightarrow \pi^+ \pi^-$ is a suitable choice to partially reconstruct as the K_S^0 daughters can be produced some distance from the IP, and kinematic constraints can be used to reconstruct the full decay without explicitly reconstructing all of the final state pions. For the remainder of this work, I will refer to $D^{*+}(2010)$ simply as D^{*+} . The decay can be entirely reconstructed with the use of conservation laws instead of relying entirely on tracks. If we allow one of the K_S^0 daughter pions to not be reconstructed, we can still find the correct 4-momentum of the K_S^0 as long as we have a track coordinate for one of its daughters, as well as the D^0 decay vertex. The D^* , D^0 and K_S^0 masses are used as constraints on the event kinematics to find the correct K_S^0 4-momentum and recover the missing track.

5.2.1 Reconstruction

In order to check whether a track corresponding to the missing pion was found, we fully reconstruct the events in `basf2`. The full reconstruction proceeds as follows:

- The final state pions are built from the tracks that pass the selection criteria, which differ depending on the particle that decayed into the pion. For instance, there are impact parameter cuts on the D^0 daughter pions as we expect them to be produced closer to the interaction region. No such criteria are enforced on the K_S^0 daughter pions as the K_S^0 is a long-lived particle. The slow pion from the $D^{*\pm}$ must have $p < 300$ MeV/ c .
- The K_S^0 is built from two oppositely-charged pairs of pions. The K_S^0 candidate must have an invariant mass within 22 MeV/ c^2 of the nominal K_S^0 mass of 497 MeV/ c^2 .
- The D^0 is reconstructed from the K_S^0 and another pion. The D^0 candidate must have an invariant mass within 44 MeV/ c^2 of the nominal D^0 mass of 1.864 GeV/ c^2 .
- A vertex fit is performed on the D^0 using TreeFitter.
- The $D^{*\pm}$ is built from the D^0 and a slow pion. The invariant mass of the $D^{*\pm}$ candidate must be less than 2.1 GeV/ c^2 .
- The momentum of the D^{*+} candidate must be greater than 2.5 GeV/ c in the CMS frame. This rejects a lot of background, and excludes any candidates that were produced in B decays (see Figure 5.4). While this does reduce the number of candidates we find, a much cleaner sample can be produced as most events that are not $c\bar{c}$ events are rejected.

A scan is then performed on the fully reconstructed events in order to get a D^{*+} mass distribution analogous to that of the partially reconstructed case. This mass distribution is referred to as the ‘found’ mass, as it is the mass recovered from events where both tracks were used in reconstruction.

The partial reconstruction proceeds in the same manner as above, however the K_S^0 is built from only a single track. The criteria on the final state particles are the same as above, however the cuts around the nominal masses of the K_S^0 , D^0 and D^{*+} are not performed in `basf2`, but after the scan has been performed. The D^{*+} mass distribution produced by the scan is the ‘recovered’ mass. Once the found and recovered mass distributions have been produced, further event selection is done. The momentum of the recovered pion must point towards detector acceptance $17^\circ \leq \theta \leq 150^\circ$. Furthermore, we require that the z -coordinate of the recovered track at the radius of the innermost SVD layer ($r_1 = 3$ cm) has to be within the detector acceptance region:

$$r_1 \cotan(150^\circ) \leq z(r = r_1) \leq r_1 \cotan(17^\circ). \quad (5.1)$$

To remove combinatorial backgrounds where the momentum of the recovered pion is much smaller than that of the used pion, we ensure the CMS frame momenta of the used pion $p_{\text{used}}^* \pi$ and the recovered pion $p_{\text{recovered}}^* \pi$ satisfy a pion momentum asymmetry condition:

$$\text{Pion momentum asymmetry} = \frac{p_{\text{used}}^* \pi - p_{\text{recovered}}^* \pi}{p_{\text{used}}^* \pi + p_{\text{recovered}}^* \pi} \geq -0.5 \quad (5.2)$$

Pion identification is not as good for low momentum or ‘slow’ pions, however we find that a pionID cut on tracks lower than 0.1 is able to remove most fake slow pions while keeping good efficiency.

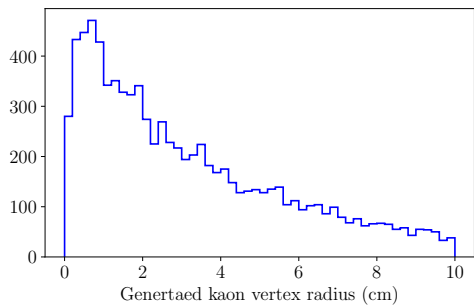


FIGURE 5.2: Generated radial distance of K_S^0 decay vertices in the channel $D^{*+} \rightarrow D^0(K_S^0 \rightarrow \pi^+\pi^-)\pi^+\pi^-$.

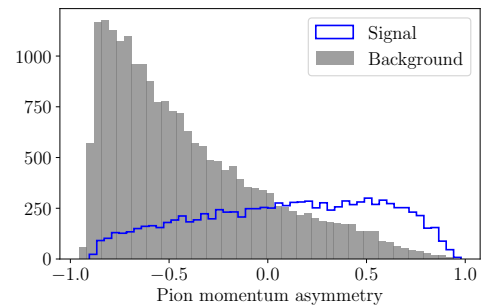


FIGURE 5.3: Pion momentum asymmetry (as defined in Equation 5.2) in signal and background MC.

We present the mass K_S^0 , D^0 , D^{*+} and found D^{*+} mass distributions in Figures 5.6 - 5.9. The reconstruction yields a very clean sample, as demonstrated by the clear mass peaks for the K_S^0 , D^0 and D^{*+} .

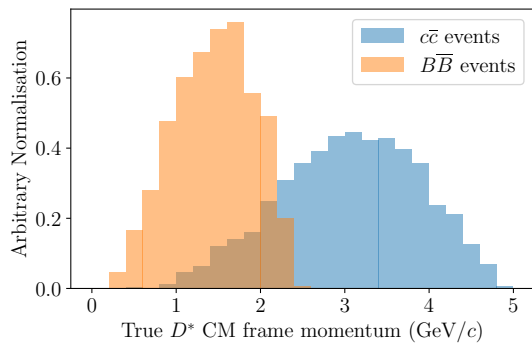


FIGURE 5.4: Centre-of-mass frame momentum distributions for signal D^* produced in $c\bar{c}$ (blue) events and D^{*+} produced from B decays (orange).

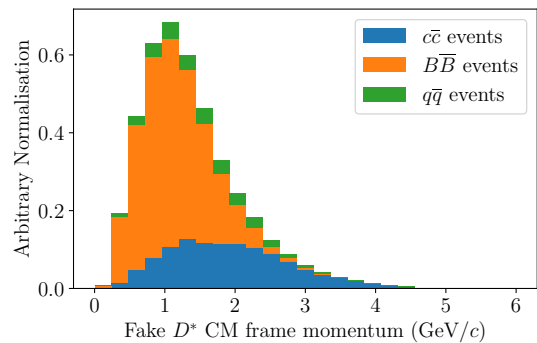
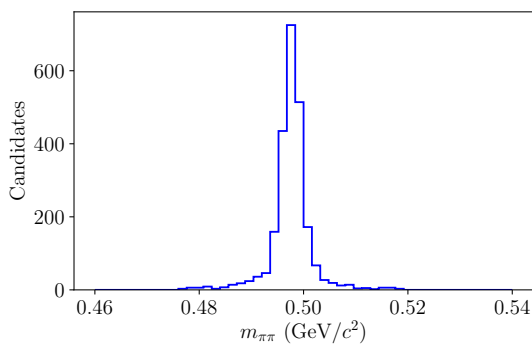
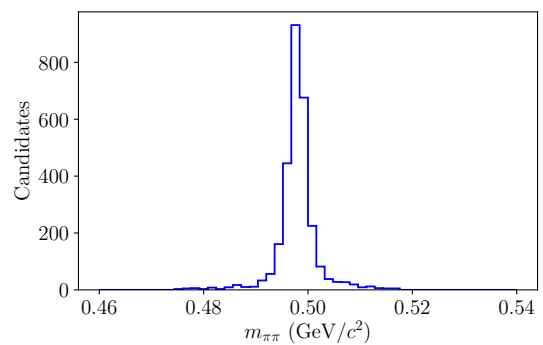


FIGURE 5.5: Centre-of-mass frame momentum distributions for combinatorial background D^* produced in $c\bar{c}$ (blue), $B\bar{B}$ (orange) and $q\bar{q}$ events (green).



(a)



(b)

FIGURE 5.6: Reconstructed K_S^0 mass in data (left) and MC (right).

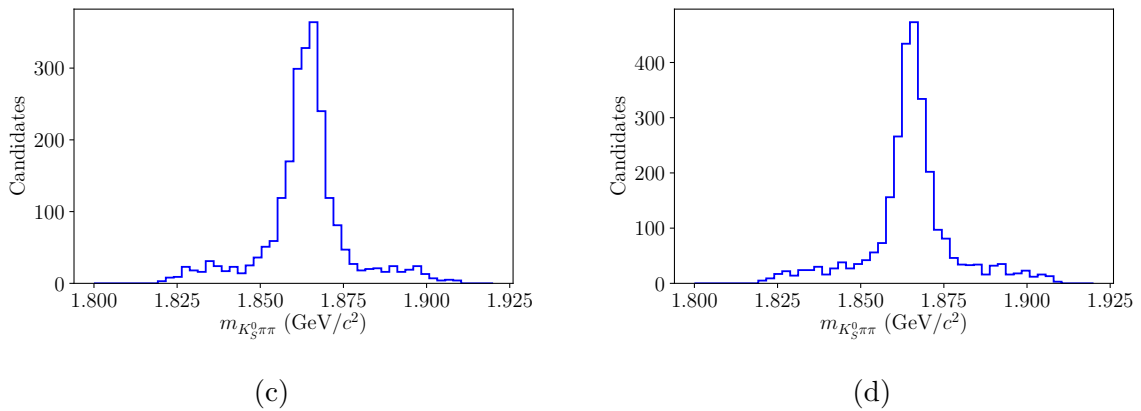


FIGURE 5.7: Reconstructed D^0 mass in data (left) and MC (right).

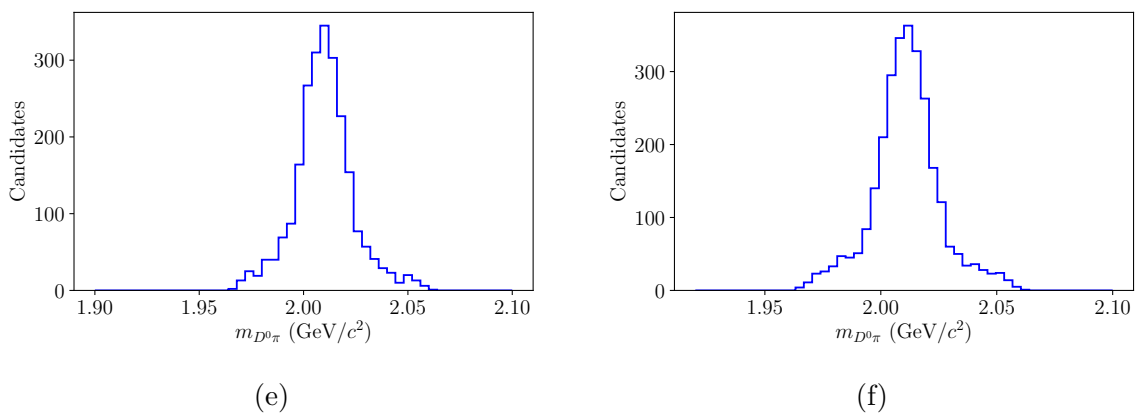


FIGURE 5.8: Reconstructed D^{*+} mass in data (left) and MC (right).

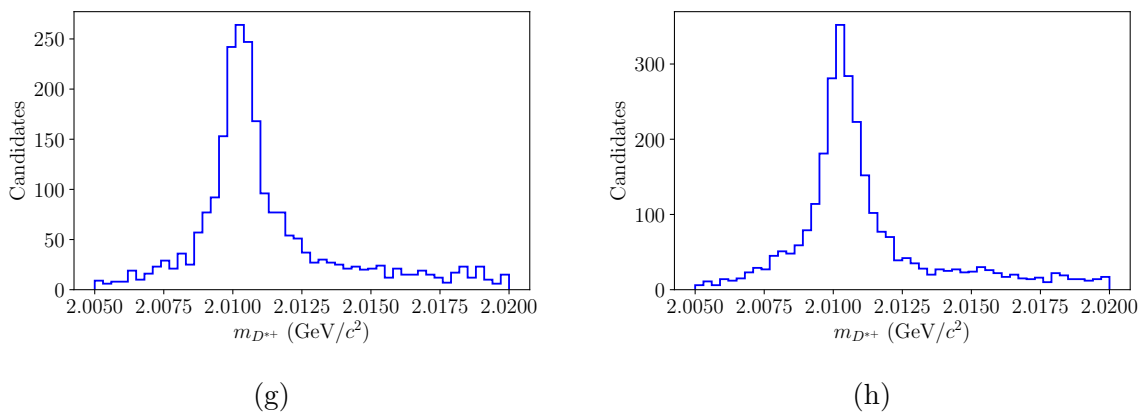


FIGURE 5.9: Found D^{*+} mass distributions in data (left) and MC (right).

5.2.2 Partial reconstruction method

The initial reconstruction done in `basf2` reconstructs the D^0 vertex using a $\pi^+\pi^-$ pair, selects tracks that could be the pion daughters of the K_S^0 , and finds low-momentum or ‘slow’ pions that could be the charged D^* daughter. We only look for slow pions daughters of the D^{*+} as the mass difference

between D^{*+} and D^0 is about $145\text{MeV}/c^2$, which means a $139.5\text{ MeV}/c^2$ pion will be produced with very low momentum in the frame of the D^{*+} .

We refer to the reconstructed K_S^0 daughter that is used to constrain the K_S^0 vertex as the ‘used track’ or ‘used pion’. Using the used pion’s track coordinate X_π and momentum \vec{p}_π , we construct a line to which we constrain the K_S^0 decay vertex coordinate $V_{K_S^0}$. We scan along this line with a scanning variable λ in the direction of the used pion momentum, ending up with a different hypothesis for $V_{K_S^0}$ for each value of λ :

$$V_{K_S^0}(\lambda) = X_\pi + \lambda\vec{p}_\pi. \quad (5.3)$$

Each value of λ corresponds to a possible decay vertex, and therefore a K_S^0 momentum direction. For each step in the scan, we define the K_S^0 momentum direction and magnitude to be \vec{k}_λ and F_λ respectively. The K_S^0 3-momentum is then given by

$$\vec{p}_{K_S^0} = F_\lambda\vec{k}_\lambda \quad (5.4)$$

The D^0 mass constraint can be used to get the momentum. The D^0 decays into three bodies; two pions and a kaon, so its 4-momentum must be the sum of the three daughter’s 4-momentum. This yields the following:

$$\begin{aligned} m_{D^0}^2 &= (P_{\pi\pi} + P_{K_S^0})^2 \\ &= m_{\pi\pi}^2 + m_{K_S^0}^2 + 2(E_{\pi\pi}\sqrt{m_{K_S^0}^2 + F_\lambda} - F_\lambda\vec{k}_\lambda \cdot \vec{p}_{\pi\pi}) \end{aligned} \quad (5.5)$$

where $P_{\pi\pi}$ is the 4-momentum of the two D^0 daughter pions. After some rearrangement, the above yields an equation quadratic in F_λ , the roots of which are given by

$$F_\lambda = \frac{\vec{p}_{\pi\pi}\vec{k}_\lambda M \pm \sqrt{\vec{p}_{\pi\pi}^2\vec{k}_\lambda^2 M^2 - (E_{\pi\pi}^2 - \vec{p}_{\pi\pi}^2\vec{k}_\lambda^2)(E_{\pi\pi}^2 m_{K_S^0}^2 - M^2)}}{E_{\pi\pi}^2 - \vec{p}_{\pi\pi}^2\vec{k}_\lambda^2} \quad (5.6)$$

where

$$M = \frac{m_{D^0}^2 - m_{K_S^0}^2 - m_{\pi\pi}^2}{2} \quad (5.7)$$

Negative solutions are discarded as F_λ is strictly positive as the lifetime of the K_S^0 must be positive.

Once the K_S^0 momenta are determined for all values of λ , one is selected based on the missing pion 4-momentum. First, the missing pion’s 4-momentum is calculated using

$$P_{\text{missing } \pi} = P_{K_S^0} - P_{\text{used } \pi}. \quad (5.8)$$

Then, the value of λ is chosen by minimising the difference $y(\lambda)$ of the missing π mass squared and the nominal π mass squared:

$$y(\lambda) = \frac{P_{\text{missing } \pi}^2}{c^2} - \frac{m_{\pi}^2}{c^4} \quad (5.9)$$

Once the K_S^0 momentum has been determined, its 4-momentum is added to that of the two D^0 daughter pions to complete the reconstruction of the D^0 .

Finally, for each reconstructed D^0 , a slow pion is added to form the D^* candidate.

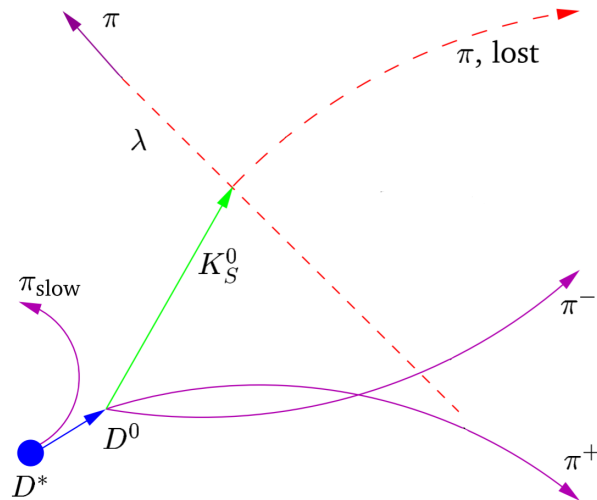


FIGURE 5.10: Schematic view of the decay chain. During partial reconstruction, only purple tracks are used. (Diagram adapted from [34]).

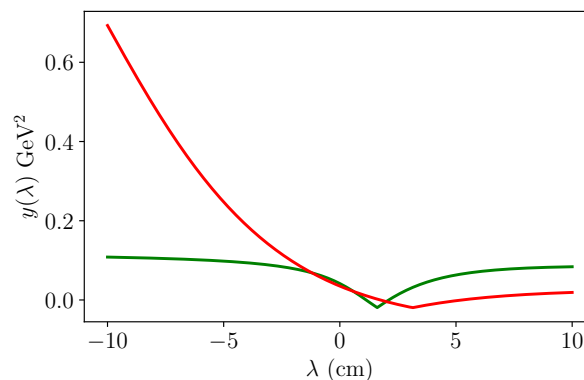


FIGURE 5.11: Squared mass difference $y(\lambda)$ distributions for two randomly chosen signal events corresponding to the red and green lines. Both lines have a clear minimum corresponding to the correct value of λ .

5.2.3 Constructing a scan

The scanning variable λ is implemented as discrete variable used in an iterative process. In order to find a good approximate solution to minimise $y(\lambda)$, λ scanned in 100 steps for values between

$\lambda_{\min} = -10$ and $\lambda_{\max} = 10$. As the used track coordinate is in centimeters and the used track momentum in the scan is a unit vector, these steps correspond to steps of 0.2 mm. Once the first scan is completed, the values of λ either side of the value where $y(\lambda)$ is minimised are chosen to be the new λ_{\min} and λ_{\max} . A 100-step scan is then performed in this new, narrower range for λ . The process zooms in on the correct solution until $|y(\lambda)| < 100 \text{ eV}^2$. With this final value of λ , the K_S^0 momentum and vertex is set and the 4-momentum of the missing pion is calculated.

5.2.4 Fitting the D^{*+} mass distribution

The recovered D^{*+} mass distribution is used to estimate signal and background yields. The signal peak corresponding to the D^{*+} mass of 2.010 GeV is fit using three functions; a ‘wide’ Gaussian, a ‘narrow’ Gaussian, and a bifurcated Gaussian. The latter was added as there is some degree of asymmetry in the signal distribution that the first two Gaussian’s cannot reproduce.

The background distribution is fit with a function of the form

$$f(m_{D^*}) = \left(1 - \exp\left(\frac{m_{D^*} - d_0}{c}\right)\right) \left(\frac{m_{D^*}}{d_0}\right)^a + b\left(\frac{m_{D^*}}{d_0} - 1\right) \quad (5.10)$$

where a, b, c , and d_0 are numerical parameters to be determined by the fit. The signal distribution is fitted separately on signal-only MC first in order to fix the ratios between widths of the Gaussians, as well as the ratio of factors with which the three signal distributions are added. Once the ratios between distributions are fixed, we allow the mean of the signal peak and the width of a single Gaussian to float during the overall fit. This preserves the shape of the signal fits but allows the different parts to scale freely with varying numbers of signal and background events and detector resolution.

r (cm)	0.4 - 3.0	3.0 - 6.0	6.0 - 9.0
Mean (GeV/ c^2)	$2.010 \pm (2.67 \times 10^{-5})$	$2.010 \pm (3.50 \times 10^{-5})$	$2.010 \pm (8.98 \times 10^{-5})$
σ_1 (MeV/ c^2)	0.45 ± 0.05	0.45 ± 0.05	0.49 ± 0.27
σ_2 (MeV/ c^2)	1.23 ± 0.12	1.15 ± 0.18	1.51 ± 0.52
σ_{3L} (MeV/ c^2)	2.41 ± 0.34	3.20 ± 1.47	3.08 ± 1.58
σ_{3R} (MeV/ c^2)	4.37 ± 0.67	4.71 ± 1.11	6.60 ± 4.86
a	0.37 ± 0.07	0.56 ± 0.11	0.50 ± 0.12
b	0.50 ± 0.06	0.34 ± 0.10	0.31 ± 0.12

TABLE 5.1: Full reconstruction signal fit parameters.

r (cm)	0.4 - 3.0	3.0 - 6.0	6.0 - 9.0
Mean (GeV/ c^2)	$2.010 \pm (1.95 \times 10^{-5})$	$2.010 \pm (2.28 \times 10^{-5})$	$2.010 \pm (4.17 \times 10^{-5})$
σ_1 (MeV/ c^2)	0.41 ± 0.04	0.38 ± 0.05	0.48 ± 0.38
σ_2 (MeV/ c^2)	1.02 ± 0.11	1.02 ± 0.18	1.12 ± 0.35
σ_{3L} (MeV/ c^2)	2.06 ± 0.19	1.68 ± 0.16	1.93 ± 0.38
σ_{3R} (MeV/ c^2)	3.65 ± 0.35	3.23 ± 0.36	3.64 ± 1.00
a	0.44 ± 0.08	0.45 ± 0.10	0.44 ± 0.26
b	0.40 ± 0.07	0.36 ± 0.08	0.45 ± 0.23

TABLE 5.2: Partial reconstruction signal fit parameters.

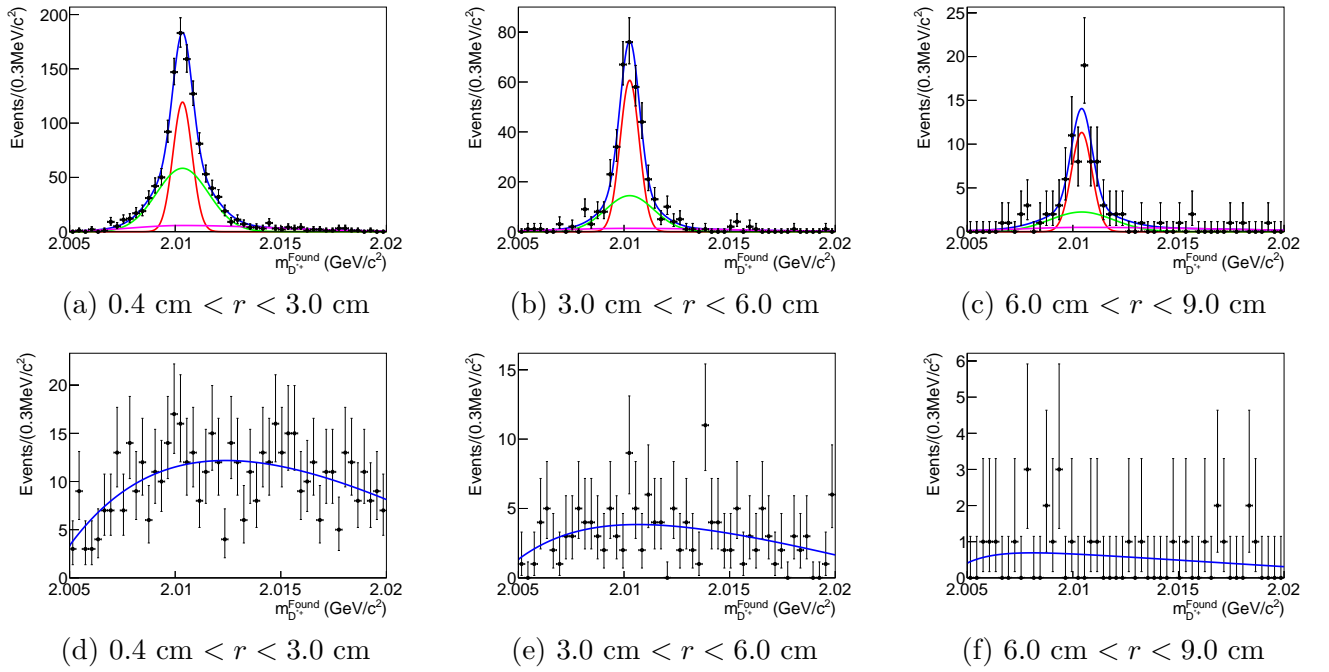


FIGURE 5.12: Fitted PDFs to signal (top row) and background (bottom row) MC distributions where the K_S^0 is reconstructed from two tracks, in three different regions of K_S^0 radial vertex displacement. These PDF definitions are subsequently used to fit the same distributions in data.

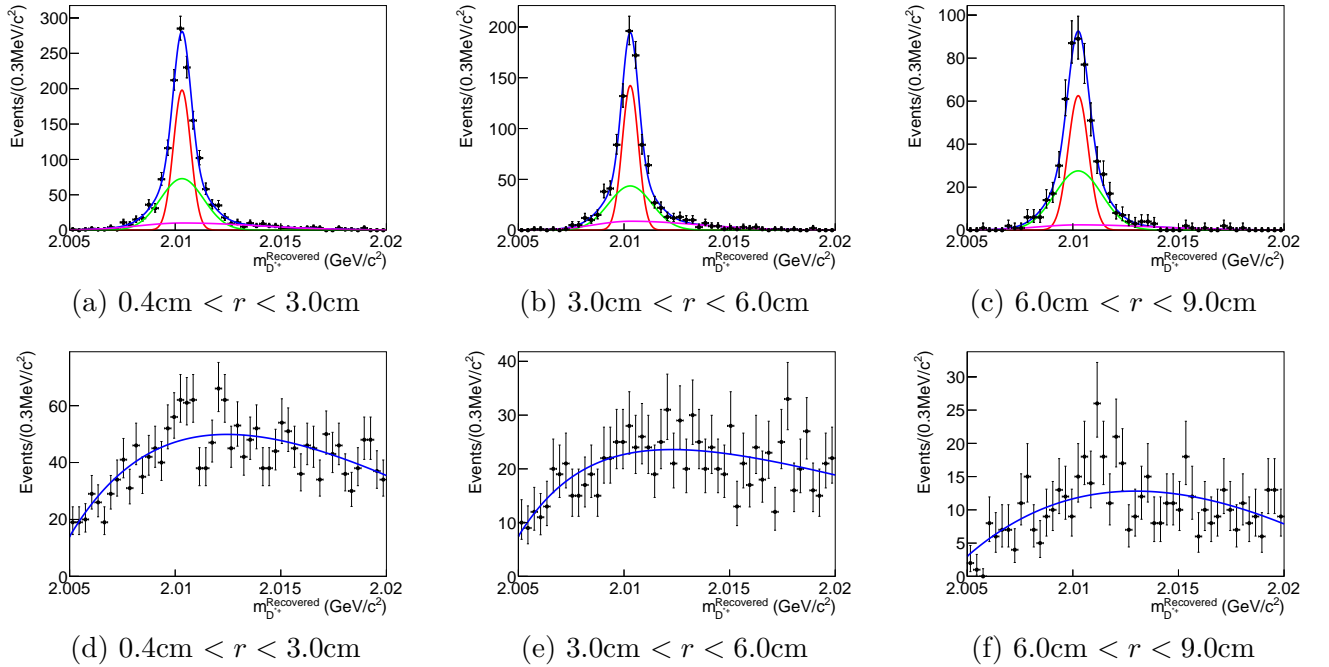


FIGURE 5.13: Fitted PDFs to signal (top row) and background (bottom row) MC distributions where the K_S^0 is reconstructed from only a single track, in three different regions of K_S^0 radial vertex displacement. These PDF definitions are subsequently used to fit the same distributions in data.

To extract track finding efficiency, we compare the number of signal events found in the fully reconstructed case to the partially reconstructed case. The number of signal events in the fully

reconstructed case is N_{Sig} , while the partially reconstructed case is N_{All} . The number of background events yielded by the fit to the recovered mass distribution is B_{Fit} .

The ratio between the number of signal events with both tracks found and the number of signal events with only one track is then given by:

$$\eta_{\text{Found}} = \frac{N_{\text{Sig}}}{N_{\text{All}}} \quad (5.11)$$

The fit yielded a signal peak with an effective width of $1.77 \text{ MeV}/c^2$ for data and about $1.52 \text{ MeV}/c^2$ for MC. The yield in the signal region is calculated by numerically integrating the fit in the region 2.009 GeV to 2.011 GeV . The error is determined from the error matrix that MINUIT[36] returns.

The dataset used for this analysis corresponds to $8764.2 \pm 1.5 \text{ pb}^{-1}$ of collisions at the $\Upsilon(4S)$ resonance. Events must be accepted by the High Level Trigger (HLT).

5.2.5 Results

This partial reconstruction method has never been used to determine tracking efficiency at high displacements. In fact, previous implementations of this method at Belle have all restricted the radius of the reconstructed K_S^0 vertex to between 0.4 cm and 3 cm . Here, we present the first measure of displaced track finding efficiency. The lower bound was designed to remove tracks from combinatorial background, while the upper bound ensures that the recovered pion crossed the SVD. We present our results for the tracking efficiency η_{Found} in Table 5.3.

Dataset	$V_{K_S^0}$ radius [cm]	Efficiency η_{Found}	S/B	True S/B from PDF definitions
MC	$0.4 < r < 3.0$	$(89.3 \pm 5.8)\%$	1.48	1.52
Data	$0.4 < r < 3.0$	$(89.0 \pm 5.5)\%$	1.67	–
MC	$3.0 < r < 6.0$	$(62.5 \pm 5.5)\%$	2.01	1.75
Data	$3.0 < r < 6.0$	$(59.2 \pm 3.8)\%$	1.51	–
MC	$6.0 < r < 9.0$	$(23.0 \pm 2.9)\%$	1.72	1.78
Data	$6.0 < r < 9.0$	$(22.5 \pm 3.1)\%$	1.34	–

TABLE 5.3: Track finding efficiency results.

Dataset	$V_{K_S^0}$ radius [cm]	Signal yield (per fb^{-1}), one track	Signal yield (per fb^{-1}), two track
MC	$0.4 < r < 3.0$	807 ± 36.2 (80.7 ± 3.6)	903 ± 42.8 (90.3 ± 4.3)
Data	$0.4 < r < 3.0$	773 ± 31.5 (88.2 ± 3.6)	869 ± 39.8 (99.2 ± 4.5)
MC	$3.0 < r < 6.0$	312 ± 20.7 (31.2 ± 2.1)	500 ± 28.6 (50.0 ± 2.9)
Data	$3.0 < r < 6.0$	267 ± 19.4 (30.5 ± 2.2)	451 ± 25.4 (51.5 ± 2.9)
MC	$6.0 < r < 9.0$	56 ± 6.1 (5.6 ± 0.6)	245 ± 16.2 (24.5 ± 1.6)
Data	$6.0 < r < 9.0$	68 ± 8.1 (7.8 ± 0.9)	302 ± 19.43 (34.5 ± 2.2)

TABLE 5.4: Caption

The track finding efficiency is calculated using the equation above, while the signal to background ratio is given by:

$$\frac{S}{B} = \frac{N_{\text{All}} - B_{\text{Fit}}}{B_{\text{Fit}}} \quad (5.12)$$

The data/MC asymmetry ($r - 1$) for the 2019 dataset in the innermost region $0.4\text{cm} < r < 3.0\text{cm}$ is

$$r - 1 = \frac{(89.0 \pm 5.5)\%}{(89.3 \pm 5.8)\%} - 1 = (-0.34 \pm 8.0)\% \quad (5.13)$$

which is compatible with 0, however the statistical error is large. This result is expected to improve significantly when a larger dataset becomes available. There is a substantial drop-off in track finding efficiency when tracks are produced at higher displacements. However, we find excellent agreement between MC and data, indicating that the efficiencies that we calculate for when reconstructing V^0 -like or long-lived particles in MC should reflect what we see in data, or at least that any discrepancies observed do not come from the tracking efficiency. We only see a maximum of 89.0% track finding efficiency even in the innermost detector region because $K_S^0 \rightarrow \pi^+\pi^-$ decays can produce slow pions, which are tracked much less effectively than pions in higher momentum regions.

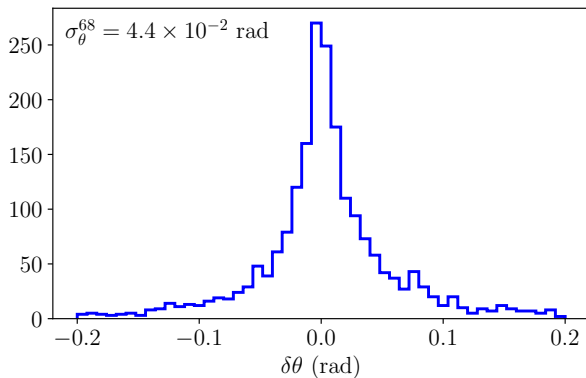


FIGURE 5.14: Difference between the found and generated polar angle of the recovered pion $\delta\theta$.

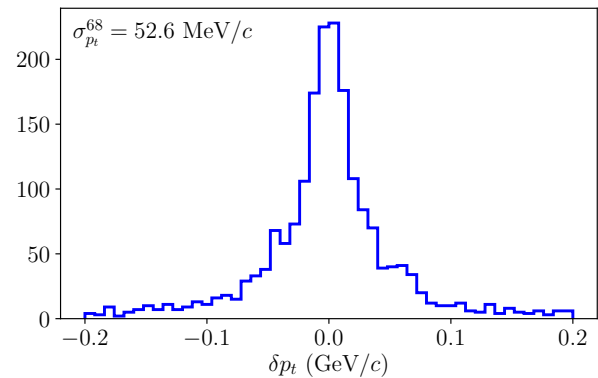
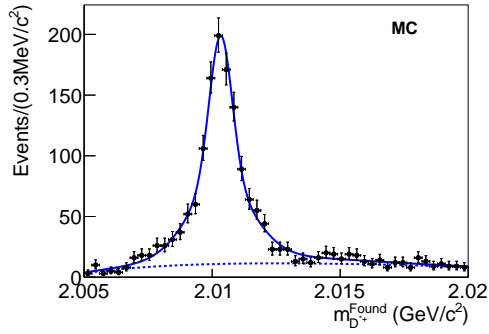


FIGURE 5.15: Difference between the found and generated transverse pion momentum of the recovered pion δp_t .

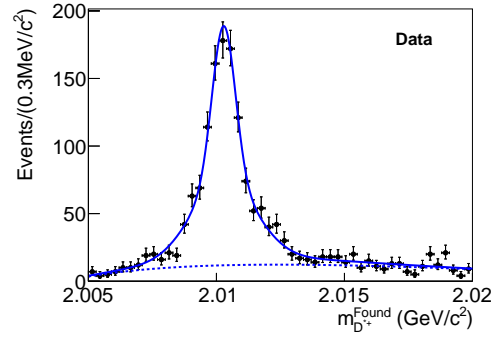
We have shown that this partial reconstruction method is suitable for extracting track finding efficiencies, and we expect results to improve in accuracy with a larger dataset. There is a clear dependency of the efficiency on the radius of the K_S^0 vertex, however small numbers of events made it impractical to either show results more finely-binned in the vertex radius or extend the radius beyond 9 cm. Extensions of this study could measure the impact of some of the cuts used more closely, for instance looking at the pionID, polar angle θ or transverse momentum p_t dependence of the result. The partial reconstruction method shows good resolution in both θ and p_t (see Figures 5.14 and 5.15). It would also be useful to the Belle II collaboration examine how tracking efficiency changes with time, as data is taken over the course of a number of months.

This track finding study result is important for novel analyses looking for long-lived particles such as what is presented in Chapter 4, as it is vital to know how track finding efficiency could impact overall reconstruction efficiency. However, the importance of this study is not only due to novel long-lived particle searches, but for any physics analyses at Belle II containing K_S^0 decays. These analyses span a variety of important topics in particle physics, including as CP violation measurements. We have shown that we expect a sizeable drop in efficiency for events with decay vertices at radii greater than 3 cm. However, we have also demonstrated that this efficiency drop is observed to be the same in

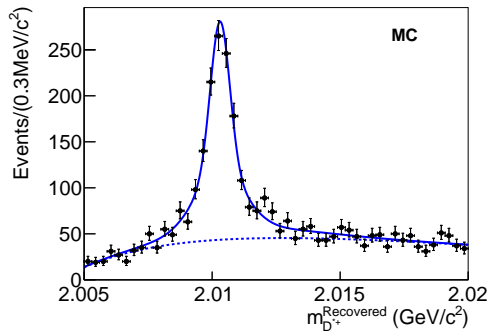
both data and MC, and therefore we can develop these analyses with confidence that our efficiencies are accurate.



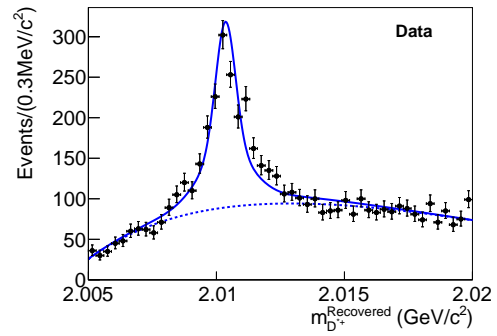
(a) Found mass, $0.4 \text{ cm} < r < 3.0 \text{ cm}$



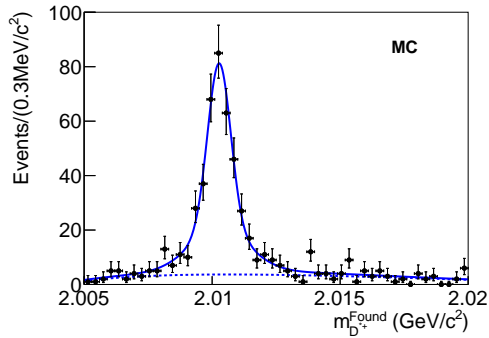
(b) Found mass, $0.4 \text{ cm} < r < 3.0 \text{ cm}$



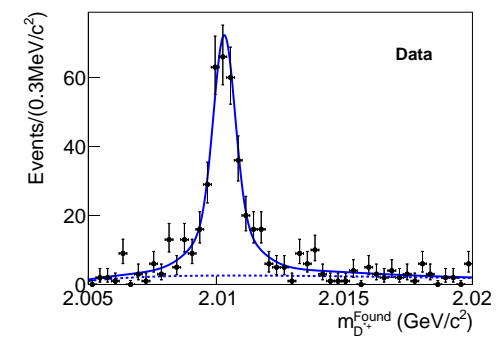
(c) Recovered mass, $0.4 \text{ cm} < r < 3.0 \text{ cm}$



(d) Recovered mass, $0.4 \text{ cm} < r < 3.0 \text{ cm}$



(e) Found mass, $3.0 \text{ cm} < r < 6.0 \text{ cm}$



(f) Found mass, $3.0 \text{ cm} < r < 6.0 \text{ cm}$

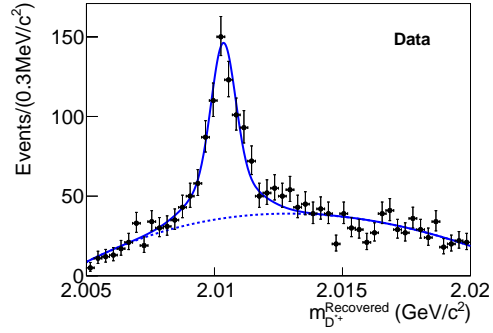
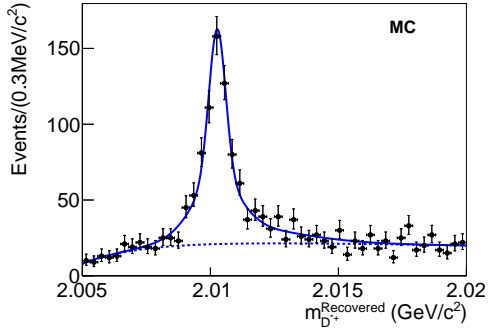
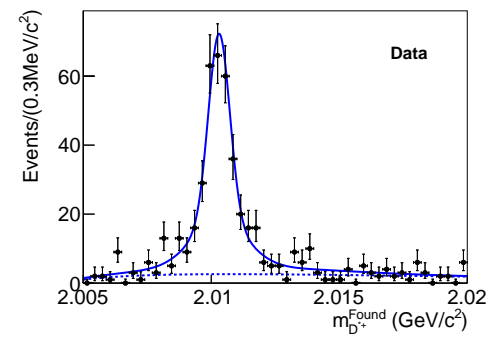
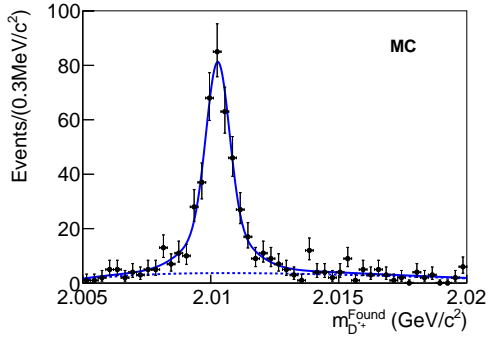
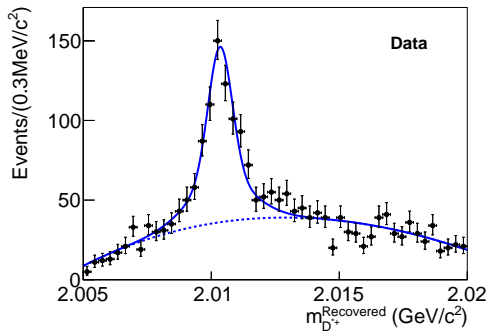
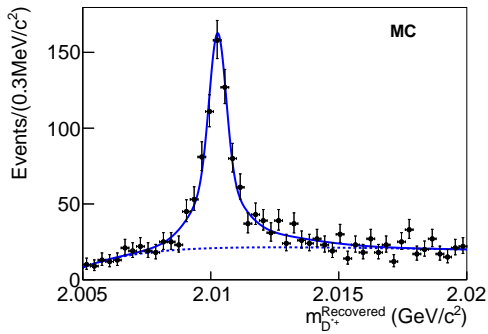
(g) Recovered mass, $3.0 \text{ cm} < r < 6.0 \text{ cm}$ (h) Recovered mass, $3.0 \text{ cm} < r < 6.0 \text{ cm}$ (i) Found mass, $6.0 \text{ cm} < r < 9.0 \text{ cm}$ (j) Found mass, $6.0 \text{ cm} < r < 9.0 \text{ cm}$ (k) Recovered mass, $6.0 \text{ cm} < r < 9.0 \text{ cm}$ (l) Recovered mass, $6.0 \text{ cm} < r < 9.0 \text{ cm}$

FIGURE 5.16: All fits to the D^{*+} mass distribution with two ('found') and one ('recovered') track(s) used, in all three regions of K_S^0 vertex radius. MC is shown on the left and data is on the right.

Chapter 6

Sensitivity to long-lived particles at Belle II

So far we have demonstrated what kind of signal a long-lived particle leaves in the detector, checked that we can accurately determine its' decay vertex, and constructed a set of selection criteria that leaves very little to no background events. Furthermore, we have used real data from Belle II experiments 7, 8 and 10 for the first time to measure track finding efficiency for tracks that originate far outside the beampipe. Using this set of results, we can provide the most accurate estimates for Belle II's sensitivity to long-lived particles to date.

6.1 Limiting factors

The upper limit on the mass of a long-lived particle that can be probed at Belle II in decays of the form $B \rightarrow MS$ depend on the mass of the meson M . A long-lived particle produced in decays to K^+ can have a mass of up to $4.78 \text{ GeV}/c^2$, while scalars produced in B^0 to \overline{D}^0 transitions are limited to $3.4 \text{ GeV}/c^2$. The lower limit of the mass we can reach is determined by the mass of the decay products we choose to look for. Throughout this work we have been assuming S decays into muon pairs, in which case its lowest possible mass would be around $212 \text{ MeV}/c^2$. If we looked for electron pairs, we could search for an even lower mass. However, detector geometry also limits the mass we can search for. A boosted long-lived particle may be able to fly outside of detector acceptance.

6.2 Dark scalar sensitivity limits

In [6], Filimonova, Schäfer and Westhoff present the branching fraction for the decay $B^+ \rightarrow K^+ S$ as

$$\begin{aligned} \mathcal{B}(B^+ \rightarrow K^+ S) &= \frac{\sqrt{2}G_F |C_{bs}|^2 (m_b + m_s)^2}{64\pi\Gamma_{B^+} m_B^3 (m_b - m_s)^2} f_0^2(m_S^2) \\ &\times (m_B^2 - m_K^2)^2 [(m_B^2 - m_K^2 - m_S^2)^2 - 4m_K^2 m_S^2]^{\frac{1}{2}} \end{aligned} \quad (6.1)$$

where Γ_{B^+} is the decay width of the B^+ , $f_0^2(m_S^2)$ is the scalar hadronic form factor at momentum transfer $q^2 = m_S^2$.

The production of dark scalars from B decays relies upon effective flavour-changing currents

$$\mathcal{L}_{\text{eff}} = \frac{C_{bq}}{v} (m_b \bar{q}^L b_R + m_q \bar{q}_R b_L) S \quad (6.2)$$

where $v \approx 246$ GeV is the Higgs vacuum expectation value and G_F is the Fermi constant. Since the fundamental couplings of the scalar are flavour diagonal and hierarchical, the production is loop-induced through the large top quark coupling. The coefficient that describes the effective coupling strength in quark transitions is a Wilson coefficient, and for the $b \rightarrow s$ transition in our decay channel of interest it is

$$C_{bs} = \frac{3\sqrt{2}G_F m_t^2}{16\pi^2} V_{tb} V_{ts}^* s_\theta + \mathcal{O}\left(\frac{m_S^2}{m_W^2}\right). \quad (6.3)$$

The higher order terms can be ignored as m_W is more than six times larger than the upper limit of m_S that the Belle II experiment is sensitive to.

The terms V_{tb} and V_{ts} are elements of the Cabibbo-Kobayashi-Maskawa (CKM) matrix, which describes the strength of flavour-changing weak interactions. Each element $V_{qq'}$ gives the relative coupling between quarks q and q' .

The scalar hadronic form factor $f_0(m_S^2)$ describes the quantum mechanical overlap between the fields of the B and K mesons as a function of the hadronic recoil between them $q^2 = m_S^2$. We calculate the form factor based on fits to lattice QCD calculations from [37], where the form factor is parameterised as a power series:

$$f_0(q^2) = \frac{1}{P_0(q^2)} \sum_{m=0}^{K-1} b_m^0 z^m(q^2, t_0), \quad (6.4)$$

$$z(q^2, t_0) = \frac{\sqrt{t_+ - q^2} - \sqrt{t_+ - t_0}}{\sqrt{t_+ - q^2} + \sqrt{t_+ - t_0}} \quad (6.5)$$

where $t_+ = (M_B + M_K)^2$, $t_0 = (M_B + M_K)(\sqrt{M_B} + \sqrt{M_K})^2$ and $P_0(q^2) = 1 - q^2/M^2$ ($M = 5.711$ GeV and comes from a lattice QCD prediction). The fit parameters $b_{0,1,2}^0 = 0.289, 0.280,$ and 0.15 are taken from a constrained three parameter ($K = 3$) fit. The distribution of the form factor is shown in Figure 6.1.

In the case where scalars decay into a lepton pair, the branching fraction is given by

$$\mathcal{B}(S \rightarrow \ell\bar{\ell}) = \frac{s_\theta^2 \Gamma_{\ell\bar{\ell}}}{\Gamma_S} = \frac{m_\ell^2 s_\theta^2 m_S}{8\pi v^2 \Gamma_S} \left(1 - \frac{4m_\ell^2}{m_S^2}\right)^{\frac{3}{2}} \quad (6.6)$$

For the case of a scalar decaying into a muon pair, the number of muons produced in the Belle II detector is given by

$$N_{\mu\bar{\mu}} = N_{B\bar{B}} \times 1.93 \mathcal{B}(B \rightarrow KS) \mathcal{B}(S \rightarrow \mu\bar{\mu}) \times \frac{1}{2} \int d\vartheta \frac{\sin(\vartheta)}{2} \left(1 - \exp\left[-\frac{1}{\beta\gamma c\tau_S} \frac{d_1^{\max}}{\sin(\vartheta)}\right]\right) \quad (6.7)$$

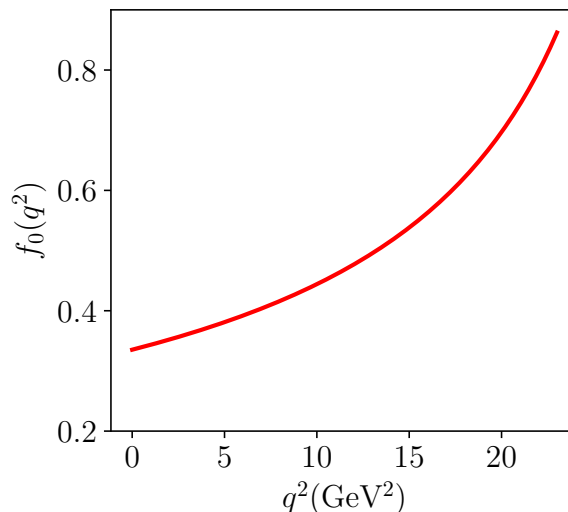


FIGURE 6.1: Calculated scalar hadronic form factor f_0 using the fit results obtained from [37].

where r is the radial distance from the interaction point of the collider and ϑ is the scalar's polar momentum direction in the rest frame of the B meson. The factor of 1.93 takes account of the different lifetimes of the B^+ and B^0 . The first branching fraction is a sum over all relevant $B \rightarrow KS$ decay channels with both neutral and charged kaons. We use $c\tau_S = \Gamma_S/c \approx \sin^{-2}\theta$ nm to approximate the nominal lifetime of S . To ensure good reconstruction efficiency of a displaced vertex, we require that the scalar decays at a radius greater than the vertex resolution of $30\mu\text{m}$. This sets the upper limit on the mixing that we can probe through a displaced vertex signature.

We use Equation 6.7 to calculate the number of displaced muon pairs we expect to see in the Belle II detector, and multiply by a function interpolated from the efficiency data in Table 4.3. The result of this is shown in Figure 6.3), and provides a more accurate estimate to the sensitivity than assuming 100% reconstruction efficiency, was done in [6].

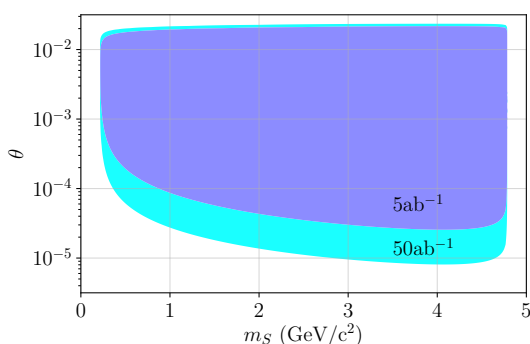


FIGURE 6.2: Predicted number of events seen in the Belle II detector from the channel $B^+ \rightarrow K^+ S(\rightarrow \mu^+ \mu^-)$. 100% reconstruction efficiency is assumed, as they were in [6]. The shaded area of parameter space is where $N_{\mu\mu} \geq 3$ for 5 ab^{-1} (purple) and 50 ab^{-1} datasets. Number of events is calculated with Equation 6.7.

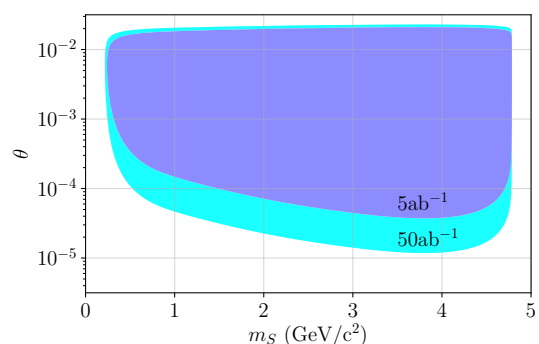


FIGURE 6.3: Predicted number of events seen in the Belle II detector from the channel $B^+ \rightarrow K^+ S(\rightarrow \mu^+ \mu^-)$. Here, we multiply the displaced dimuon yield $N_{\mu\mu}$ by the reconstruction efficiency found in Chapter 4. The shaded area of parameter space is where $N_{\mu\mu} \geq 3$ for 5 ab^{-1} (purple) and 50 ab^{-1} datasets.

We choose $N_{\mu\mu}$ as the minimum number of signal events expect to see to claim sensitivity as under the assumption there is zero background, 3 events are statistically significant enough to be of interest (although not enough for the discovery threshold of 5σ). In Figure 6.3, we show the region of parameter space where we expect at least 3 signal events, factoring in the efficiency and its mass dependence as discussed in Chapter 4. With zero background, we can probe the product of branching fractions $\mathcal{B}(B^+ \rightarrow K^+ S)\mathcal{B}(S \rightarrow \mu^+\mu^-)$ down to values of 1.8×10^{-9} for $m_S = 2 \text{ GeV}/c^2$. The sensitivity is lower in the low mass region the decay products of S are less likely to be found within the detector acceptance. The sensitivity region shrinks dramatically as m_S approaches $2m_\mu$ as lighter scalars are more highly boosted, and their decay products less likely to be seen in the detector.

The results show that Belle II can probe mixing angles θ down to values of approximately 1.2×10^{-5} for m_S of about $3.8 \text{ GeV}/c^2$, with sensitivity to θ of the order 10^{-5} for most of the possible mass range, with sensitivity only dramatically dropped off at very low masses. It will take several years for Belle II to collect 50 ab^{-1} of data. However there is a possibility to conduct a search using 10% of the total planned dataset, as with only 5 ab^{-1} , mixing angles down to approximately 3.8×10^{-5} can still be probed (for $m_S \approx 3.8 \text{ GeV}/c^2$). As such, we do not need to wait for the full Belle II dataset to become available to start searching for new long-lived particles in data.

Chapter 7

Conclusion

In this thesis, we have demonstrated that a novel analysis searching for new long-lived particles is feasible at the Belle II experiment. Reconstruction efficiencies are estimated for a number of possible event topologies, and we demonstrated how we can expect little to no background in such a search. Reconstruction efficiency for the channel $\mathcal{B}(B^+ \rightarrow K^+ S)\mathcal{B}(S \rightarrow \mu^+ \mu^-)$ can be as high as 46%, depending on the mass of S . Furthermore, we provide the first track finding efficiency measurement for tracks originating from a displaced vertex using data from Belle II. The measured track finding efficiency in data was $(89.0 \pm 5.5)\%$ in the region $0.4 \text{ cm} < r < 3.0 \text{ cm}$, $(59.2 \pm 3.8)\%$ in the region $3.0 \text{ cm} < r < 6.0 \text{ cm}$ and $(22.5 \pm 3.1)\%$ in the region $6.0 \text{ cm} < r < 9.0 \text{ cm}$. This study showed very good agreement between MC and data, and provided new insights into the behaviour of the tracking system. We used these results to give the most up-to-date estimate of Belle II's sensitivity to long-lived particles. With the full planned dataset of 50 ab^{-1} , Belle II is sensitivity to mixing angles θ down to 10^{-5} , two orders of magnitude lower than mixing angles that have been previously probed in the few GeV/c^2 mass range.

The lifetime frontier is an exciting area to search to conduct searches for new particles and physics beyond the standard model. We have demonstrated what decays of long-lived particles could look like in the Belle II detector and shown for what combination of masses and lifetimes we expect a long-lived particle to decay within the detector. Furthermore, we have developed a set of selection criteria used for reconstructing two specific channels containing new long-lived particles, estimating reconstruction efficiency and setting upper limits on the expected number of background events we would observe in a search for these channels.

Most importantly, we performed the first ever tracking study designed to measure track finding efficiency based on the radial distance of a track's production vertex, an vital aspect of the detector to understand when searching for long-lived particles. This study was developed on MC and performed on Belle II's 2019 dataset, showing good agreement between the long-lived particles in MC and data. Furthermore, we can extend the study to measure tracking efficiency against a number of other variables such as the K_S^0 momentum or polar angle. We expect that the results of this study will improve when more data becomes available, allowing us to not only greater statistics for the measurements we performed in this work, but access to a meaningful amount of displaced K_S^0 vertices that occur at greater radii than were used here.

I hope to continue to refine the work presented here by updating the tracking study with a larger dataset and contributing to any future searches for long-lived particles at Belle II.

Bibliography

- [1] F. Zwicky. On the Masses of Nebulae and of Clusters of Nebulae. *Astrophys. J.*, 86:217, October 1937. doi: 10.1086/143864.
- [2] T.S. van Albada et al. The Distribution of Dark Matter in the Spiral Galaxy NGC-3198. *Astrophys. J.*, 295:305–313, 1985. doi: 10.1086/163375.
- [3] M. Markevitch et al. Direct constraints on the Dark Matter Self-Interaction Cross Section from the Merging Galaxy Cluster 1e 0657-56. *The Astrophysical Journal*, 606(2):819–824, May 2004. ISSN 1538-4357. doi: 10.1086/383178. URL <http://dx.doi.org/10.1086/383178>.
- [4] Douglas Clowe et al. Weak-Lensing Mass Reconstruction of the Interacting Cluster 1E 0657-558: Direct Evidence for the Existence of Dark Matter. *The Astrophysical Journal*, 604(2):596–603, Apr 2004. ISSN 1538-4357. doi: 10.1086/381970. URL <http://dx.doi.org/10.1086/381970>.
- [5] G. Aad et al. Observation of a new particle in the search for the Standard Model Higgs boson with the ATLAS detector at the LHC. *Physics Letters B*, 716(1):1–29, Sep 2012. ISSN 0370-2693. doi: 10.1016/j.physletb.2012.08.020. URL <http://dx.doi.org/10.1016/j.physletb.2012.08.020>.
- [6] Anastasiia Filimonova et al. Probing dark sectors with long-lived particles at Belle II, 2019. URL <https://arxiv.org/abs/1911.03490>.
- [7] G. Alonso-Álvarez et al. Axion couplings to electroweak gauge bosons. *The European Physical Journal C*, 79(3), Mar 2019. ISSN 1434-6052. doi: 10.1140/epjc/s10052-019-6732-5. URL <http://dx.doi.org/10.1140/epjc/s10052-019-6732-5>.
- [8] Eder Izaguirre et al. Searching for Axion like Particles in Flavor-Changing Neutral Current Processes. *Physical Review Letters*, 118(11), Mar 2017. ISSN 1079-7114. doi: 10.1103/physrevlett.118.111802. URL <http://dx.doi.org/10.1103/PhysRevLett.118.111802>.
- [9] Daniel Aloni et al. Coupling QCD-Scale Axionlike Particles to Gluons. *Physical Review Letters*, 123(3), Jul 2019. ISSN 1079-7114. doi: 10.1103/physrevlett.123.031803. URL <http://dx.doi.org/10.1103/PhysRevLett.123.031803>.
- [10] Martin Bauer et al. Collider probes of axion-like particles. *Journal of High Energy Physics*, 2017(12), Dec 2017. ISSN 1029-8479. doi: 10.1007/jhep12(2017)044. URL [http://dx.doi.org/10.1007/JHEP12\(2017\)044](http://dx.doi.org/10.1007/JHEP12(2017)044).
- [11] Eder Izaguirre et al. New electron beam-dump experiments to search for MeV to few-GeV dark matter. *Physical Review D*, 88(11), Dec 2013. ISSN 1550-2368. doi: 10.1103/physrevd.88.114015. URL <http://dx.doi.org/10.1103/PhysRevD.88.114015>.
- [12] E. Kou. (Private Communication), 2020.

- [13] Eugenia Maria Teresa Irene Puccio. Lepton-number violation in B decays at BaBar, 2013.
- [14] Ivan Heredia de la Cruz. The Belle II experiment: fundamental physics at the flavor frontier. *Journal of Physics: Conference Series*, 761:012017, Oct 2016. ISSN 1742-6596. doi: 10.1088/1742-6596/761/1/012017. URL <http://dx.doi.org/10.1088/1742-6596/761/1/012017>.
- [15] H. J. Hyun et al. Search for a Low Mass Particle Decaying into $\mu^+\mu^-$ in $B^0 \rightarrow K^{*0}X$ and $B^0 \rightarrow \rho^0 X$ at Belle. *Physical Review Letters*, 105(9), Aug 2010. ISSN 1079-7114. doi: 10.1103/physrevlett.105.091801. URL <http://dx.doi.org/10.1103/PhysRevLett.105.091801>.
- [16] J.P. Lees et al. Search for Long-Lived Particles in e^+e^- Collisions. *Physical Review Letters*, 114(17), Apr 2015. ISSN 1079-7114. doi: 10.1103/physrevlett.114.171801. URL <http://dx.doi.org/10.1103/PhysRevLett.114.171801>.
- [17] D. Liventsev and others. Search for heavy neutrinos at Belle. *Physical Review D*, 87(7), Apr 2013. ISSN 1550-2368. doi: 10.1103/physrevd.87.071102. URL <http://dx.doi.org/10.1103/PhysRevD.87.071102>.
- [18] R. Aaij et al. Search for Hidden-Sector Bosons in $B^0 \rightarrow K^{*0} \mu^+ \mu^-$ Decays. *Physical Review Letters*, 115(16), Oct 2015. ISSN 1079-7114. doi: 10.1103/physrevlett.115.161802. URL <http://dx.doi.org/10.1103/PhysRevLett.115.161802>.
- [19] R. Aaij and others. Search for long-lived scalar particles in $B^0 \rightarrow K^0 \chi(\mu^+ \mu^-)$ decays. *Physical Review D*, 95(7), Apr 2017. ISSN 2470-0029. doi: 10.1103/physrevd.95.071101. URL <http://dx.doi.org/10.1103/PhysRevD.95.071101>.
- [20] F. Bergsma et al. Search for Axion Like Particle Production in 400-GeV Proton - Copper Interactions. *Phys. Lett.*, 157B:458–462, 1985. doi: 10.1016/0370-2693(85)90400-9.
- [21] J Beacham et al. Physics beyond colliders at CERN: beyond the Standard Model working group report. *Journal of Physics G: Nuclear and Particle Physics*, 47(1):010501, Dec 2019. ISSN 1361-6471. doi: 10.1088/1361-6471/ab4cd2. URL <http://dx.doi.org/10.1088/1361-6471/ab4cd2>.
- [22] Matthew J. Dolan, Torben Ferber, Christopher Hearty, Felix Kahlhoefer, and Kai Schmidt-Hoberg. Revised constraints and Belle II sensitivity for visible and invisible axion-like particles. *Journal of High Energy Physics*, 2017(12), Dec 2017. ISSN 1029-8479. doi: 10.1007/jhep12(2017)094. URL [http://dx.doi.org/10.1007/JHEP12\(2017\)094](http://dx.doi.org/10.1007/JHEP12(2017)094).
- [23] E Kou, P Urquijo, and others. The Belle II Physics Book. *Progress of Theoretical and Experimental Physics*, 2019(12), Dec 2019. ISSN 2050-3911. doi: 10.1093/ptep/ptz106. URL <http://dx.doi.org/10.1093/ptep/ptz106>.
- [24] M. Metcalf et al. A split field magnet geometry fit program, NICOLE, 2 1973.
- [25] Wouter D. Hulsbergen. Decay chain fitting with a Kalman filter. *Nuclear Instruments and Methods in Physics Research Section A: Accelerators, Spectrometers, Detectors and Associated Equipment*, 552(3):566–575, Nov 2005. ISSN 0168-9002. doi: 10.1016/j.nima.2005.06.078. URL <http://dx.doi.org/10.1016/j.nima.2005.06.078>.
- [26] Rolf Luchsinger and Christoph Grab. Vertex reconstruction by means of the method of Kalman filter. *Comput. Phys. Commun.*, 76:263–280, 1993. doi: 10.1016/0010-4655(93)90055-H.
- [27] J. F. Krohn, P. Urquijo, et al. Global Decay Chain Vertex Fitting at B-Factories, 2019. URL <https://arxiv.org/abs/1901.11198>.

- [28] M. Tanabashi et al. Review of Particle Physics. *Phys. Rev. D*, 98:030001, Aug 2018. doi: 10.1103/PhysRevD.98.030001. URL <https://link.aps.org/doi/10.1103/PhysRevD.98.030001>.
- [29] D.J. Lange. The EvtGen particle decay simulation package. *Nucl. Instrum. Meth. A*, 462: 152–155, 2001. doi: 10.1016/S0168-9002(01)00089-4.
- [30] T. Kuhr et al. The Belle II Core Software. *Computing and Software for Big Science*, 3(1), Nov 2018. ISSN 2510-2044. doi: 10.1007/s41781-018-0017-9. URL <http://dx.doi.org/10.1007/s41781-018-0017-9>.
- [31] S. Agostinelli et al. Geant4 — A Simulation Toolkit. *Nuclear Instruments and Methods in Physics Research Section A: Accelerators, Spectrometers, Detectors and Associated Equipment*, 506(3):250 – 303, 2003. ISSN 0168-9002. doi: [https://doi.org/10.1016/S0168-9002\(03\)01368-8](https://doi.org/10.1016/S0168-9002(03)01368-8). URL <http://www.sciencedirect.com/science/article/pii/S0168900203013688>.
- [32] T. Bilka et al. Demonstrator of the Belle II Online Tracking and Pixel Data Reduction on the High Level Trigger System. *IEEE Transactions on Nuclear Science*, 62(3):1155–1161, Jun 2015. ISSN 1558-1578. doi: 10.1109/tns.2015.2419879. URL <http://dx.doi.org/10.1109/TNS.2015.2419879>.
- [33] Belle II Tracking Group. Track Finding at Belle II, 2020.
- [34] P. Koppenburg. A Measurement of the Track Finding Efficiency Using Partially Reconstructed D^* Decays, Belle Internal, Belle Note 621, 2003.
- [35] B. Bhuyan. High p_t Tracking Efficiency Using Partially Reconstructed D^* Decays, Belle Internal, Belle Note 1165, 2010.
- [36] Fred James and Matthias Winkler. MINUIT User’s Guide, 6 2004.
- [37] Jon A. Bailey et al. $B \rightarrow K\ell\ell$ decay form factors from three-flavor lattice QCD. *Physical Review D*, 93(2), Jan 2016. ISSN 2470-0029. doi: 10.1103/physrevd.93.025026. URL <http://dx.doi.org/10.1103/PhysRevD.93.025026>.